The ASAS-SN catalogue of variable stars I: *The Serendipitous Survey*

T. Jayasinghe,[1,2]★ C. S. Kochanek,[1,2] K. Z. Stanek,[1,2] B. J. Shappee,[3]
T. W.-S. Holoien,[4] Toda A. Thompson,[1,2] J. L. Prieto,[5,6] Subo Dong,[7] M. Pawlak,[8]
J. V. Shields,[1] G. Pojmanski,[9] S. Otero,[10] C. A. Britt[11] and D. Will[1,11]

[1]*Department of Astronomy, The Ohio State University, 140 West 18th Avenue, Columbus, OH 43210, USA*
[2]*Center for Cosmology and Astroparticle Physics, The Ohio State University, 191 W. Woodruff Avenue, Columbus, OH 43210, USA*
[3]*Institute for Astronomy, University of Hawaii, 2680 Woodlawn Drive, Honolulu, HI 96822,USA*
[4]*Carnegie Observatories, 813 Santa Barbara Street, Pasadena, CA 91101, USA*
[5]*Núcleo de Astronomía de la Facultad de Ingeniería y Ciencias, Universidad Diego Portales, Av. Ejército 441, Santiago, Chile*
[6]*Millennium Institute of Astrophysics, Santiago, Chile*
[7]*Kavli Institute for Astronomy and Astrophysics, Peking University, Yi He Yuan Road 5, Hai Dian District, China*
[8]*Institute of Theoretical Physics, Faculty of Mathematics and Physics, Charles University in Prague, Czech Republic*
[9]*Warsaw University Observatory, Al Ujazdowskie 4, 00-478 Warsaw, Poland*
[10]*The American Association of Variable Star Observers, 49 Bay State Road, Cambridge, MA 02138, USA*
[11]*ASC Technology Services, 433 Mendenhall Laboratory, 125 South Oval Mall, Columbus, OH 43210, USA*

ABSTRACT

The All-Sky Automated Survey for Supernovae (ASAS-SN) is the first optical survey to routinely monitor the whole sky with a cadence of $\sim$2–3 d down to $V \lesssim 17$ mag. ASAS-SN has monitored the whole sky since 2014, collecting $\sim$100–500 epochs of observations per field. The *V*-band light curves for candidate variables identified during the search for supernovae are classified using a random forest classifier and visually verified. We present a catalogue of 66 179 bright, new variable stars discovered during our search for supernovae, including 27 479 periodic variables and 38 700 irregular variables. *V*-band light curves for the ASAS-SN variables are available through the ASAS-SN variable stars data base (https://asas-sn.osu.edu/variables). The data base will begin to include the light curves of known variable stars in the near future along with the results for a systematic, all-sky variability survey.

Key words: catalogues – surveys – binaries: eclipsing – stars: variables: general.

1 INTRODUCTION

The dream of observing the entire sky all the time is not new – indeed, already in 1906, Pickering 'wanted to test the constancy' of the brightest 50 million stars (see Sobel 2017). That desire was clearly motivated by the excellent results obtained by the Harvard variable stars research group (e.g. Leavitt & Pickering 1904; Leavitt 1908; Leavitt & Pickering 1912; Payne Gaposchkin & Gaposchkin 1938), which for many years dominated this field of study. Paczyński (2000) discussed the importance of all-sky variability surveys and advocated for the research that could be carried out with small telescopes, a principle out of which the All-Sky Automated Survey (ASAS; Pojmanski 2002) and the All-Sky Automated Survey for Supernovae (ASAS-SN, Shappee et al. 2014; Kochanek et al. 2017) originated.

ASAS-SN is the first ground-based survey to monitor the entire visible sky to a depth of $V \lesssim 17$ mag on a regular basis. ASAS

shared a similar goal at $V \lesssim 14$ mag, and data from the ASAS project for declinations $\delta < 28$ deg (Pojmanski 2002, 2003; Pojmanski & Maciejewski 2004, 2005; Pojmanski, Pilecki & Szczygiel 2005) have been used extensively. While the current ASAS-SN data were obtained on a cadence of 2-3 d, ASAS-SN has recently added three new ASAS-SN units (each consisting of four telescopes) at CTIO, Chile ('Bohdan Paczynski'), McDonald Observatory, Texas ('Henrietta Leavitt'), and the South African Astrophysical Observatory, South Africa ('Cecilia Payne-Gaposchkin'), which has significantly improved cadence. These new units use the SDSS *g*-band filter. The ASAS-SN telescopes are hosted by the Las Cumbres Observatory (LCO; Brown et al. 2013).

Modern surveys such as ASAS (Pojmanski 2002), the Optical Gravitational Lensing Experiment (OGLE; Udalski 2003), the Northern Sky Variability Survey (Woźniak et al. 2004), MACHO (Alcock et al. 1997), EROS (Derue et al. 2002), Pan-STARRS1 (Chambers et al. 2016), the Palomar Transient Factory (Law et al. 2009), and the Catalina Real-Time Transient Survey (Drake et al. 2014) have been very productive and have collectively discovered $\sim 10^6$ variables . The study of variable stars has led to many key

★ E-mail: jayasinghearachchilage.1@osu.edu

astrophysical insights governing stellar theory, multiplicity, and cosmology (see Zhevakin 1963; Payne-Gaposchkin 1978; Torres, Andersen & Giménez 2010, and references therein).

ASAS-SN has focused on the detection of bright supernovae with minimal observational bias (e.g. Holoien et al. 2017). However, many other transient and variable sources have been discovered during this process. These include roughly ∼90 000 candidate variable sources that were flagged during the search for supernovae. In this work, we detail the steps taken to classify these variables and create a catalogue of 66 179 previously undiscovered variables. In Section 2, we discuss the ASAS-SN observations and data reduction leading to the production of light curves for the variable sources. Section 3 presents the variability classification procedure based on random forest classification models. We discuss the catalogue and our results in Section 4 and present a summary of our work in Section 5.

2 OBSERVATIONS AND DATA REDUCTION

This catalogue was compiled using observations taken by the 'Brutus' (Haleakala, Hawaii) and 'Cassius' (CTIO, Chile) quadruple telescopes between 2013 and 2017 with ∼100–500 epochs of observation for each field to a depth of $V \lesssim 17$ mag. The field of view of a single ASAS-SN camera is 4.5 deg^2, the pixel scale is 8.0 arcsec, and the full width at half-maximum (FWHM) is ∼2 pixels. The ASAS-SN cameras capture three 90 s images for every epoch which are merged to improve the signal-to-noise ratio (S/N). ASAS-SN saturates at ∼10–11 mag depending on the camera and image position (Kochanek et al. 2017).

ASAS-SN is primarily a transient search and makes use of the ISIS image subtraction pipeline (Alard & Lupton 1998; Alard 2000) to process images. For the variable light curves, we performed aperture photometry on the difference images using the IRAF APPHOT package and calibrated the results using the AAVSO Photometric All-Sky Survey (APASS; Henden et al. 2015). We extracted light curves for the variable sources using a 2 pixel radius aperture. We rejected images taken in poor weather conditions, images that were out of focus with FWHM >2 pixels, images that had poor astrometric solutions, and images where the variable source is within 0.2 deg of a detector edge.

Since ASAS-SN first began its search for supernovae in 2013 (Shappee et al. 2014), previously undiscovered variable objects were flagged as candidates for variable stars. This list was cleaned of sources with bad photometry, inadequately sampled light curves ($N < 30$ epochs), and inaccurate astrometry, ultimately resulting in the list of ∼80 000 potentially variable sources we analyse here.

The sky is divided into fields corresponding to the field of view of a camera. The four cameras in a single mount have overlapping fields of view, and equatorial fields can be observed by both units. Thus, over ∼45 per cent of the variable sources have photometry from two or more cameras. Calibrated light curves are extracted for each camera independently, and there can be small calibration offsets between them. For each source, the camera with the largest number of measurements is considered the primary. We consider other cameras only if they have made at least 50 measurements, to ensure that sufficient phase coverage is available for periodic variables. The photometry from each secondary camera is offset by the differences between the light curve medians for the secondary camera and the primary camera. This method works well for low-amplitude variables, but can work poorly compared to the photometric uncertainties for high-amplitude, long-period variables.

Uncertainties estimated by local photon counting statistics tend to underestimate the light-curve uncertainties. We use a procedure similar to Hartman et al. (2004) to rescale these uncertainty estimates. We used ∼35 000 sources from the APOGEE (Holtzman et al. 2015) survey for this process. The reduced χ^2 statistic,

$$\frac{\chi^2}{N_{\text{dof}}} = \frac{1}{N-1} \sum_{i=1}^{N} \left(\frac{V_i - \overline{V}}{\sigma_i} \right)^2 , \tag{1}$$

is calculated for each source, where V_i is the *V*-band magnitude for epoch *i*, $\overline{V}$ is the mean *V*-band magnitude, and σ_i is the formal error of the magnitude measurement. Fig. 1 shows the χ^2/N_{dof} distribution for the APOGEE stars. We find the usual pattern that errors are underestimated and that the fractional underestimates are larger for brighter stars. We fit an exponential,

$$f(\overline{V}) = A e^{-B\overline{V}} + C , \tag{2}$$

with $A = 4.98 \times 10^2$, $B = 4.64 \times 10^{-1}$, and $C = 6.31 \times 10^{-2}$ to the observed $\log(\chi^2/N_{\text{dof}})$ versus $\overline{V}$ distribution. To correct the errors in the light curves, we multiply the formal magnitude errors by $(10^{f(\overline{V})})^{\frac{1}{2}}$. The results of this correction are illustrated in the bottom panel in Fig. 1.

3 VARIABILITY CLASSIFICATION

Here, we describe the procedure we took to classify the variable sources. In Section 3.1, we describe the procedure we took to cross-match our list of variables against catalogues of discovered variables. We describe our approach to derive periods for these sources in Section 3.2 and the first step we took to classify these variables in Section 3.3. We discuss our final random forest classifier model in Section 3.4.

3.1 Cross-matches to catalogues

Despite the relatively large pixel scale of ∼8 arcsec, ASAS-SN's typical astrometric error is ∼1 arcsec. We update the coordinates of the variables detected in the ASAS-SN pipeline to those of a Two Micron All Sky Survey (2MASS, Skrutskie et al. 2006), UCAC4 (Zacharias et al. 2013), NOMAD (Zacharias et al. 2004), USNOB1.0 (Monet et al. 2003) or PPMXL (Roeser, Demleitner & Schilbach 2010) star of the correct magnitude within 10.0 arcsec of the ASAS-SN coordinate. This also provides near-infrared and optical colours for use in classification. We find that 99 per cent of the new variables are within 5.2 arcsec of such a catalogued star.

We matched our list of variables to the International Variable Star Index (VSX; Watson, Henden & Price 2006) and the General Catalogue of Variable Stars (GCVS; Samus et al. 2017) catalogues available in 2017 October, with a matching radius of 16.0 arcsec, to identify previously discovered variables. The VSX catalogue is likely the most complete catalogue of known variables in the modern era (Watson et al. 2006), and includes variables discovered by a large number of surveys. At the time of the matching the VSX catalogue contained ∼460 000 variables. We also match our variables to the recent OGLE-IV catalogues of eclipsing binaries in the Magellanic clouds (Pawlak et al. 2016) and the Galactic bulge (Soszyński et al. 2016), along with the OGLE-IV catalogue of Cepheids in the Magellanic clouds (Soszyński et al. 2015) as these have not yet been merged with the VSX catalogue.
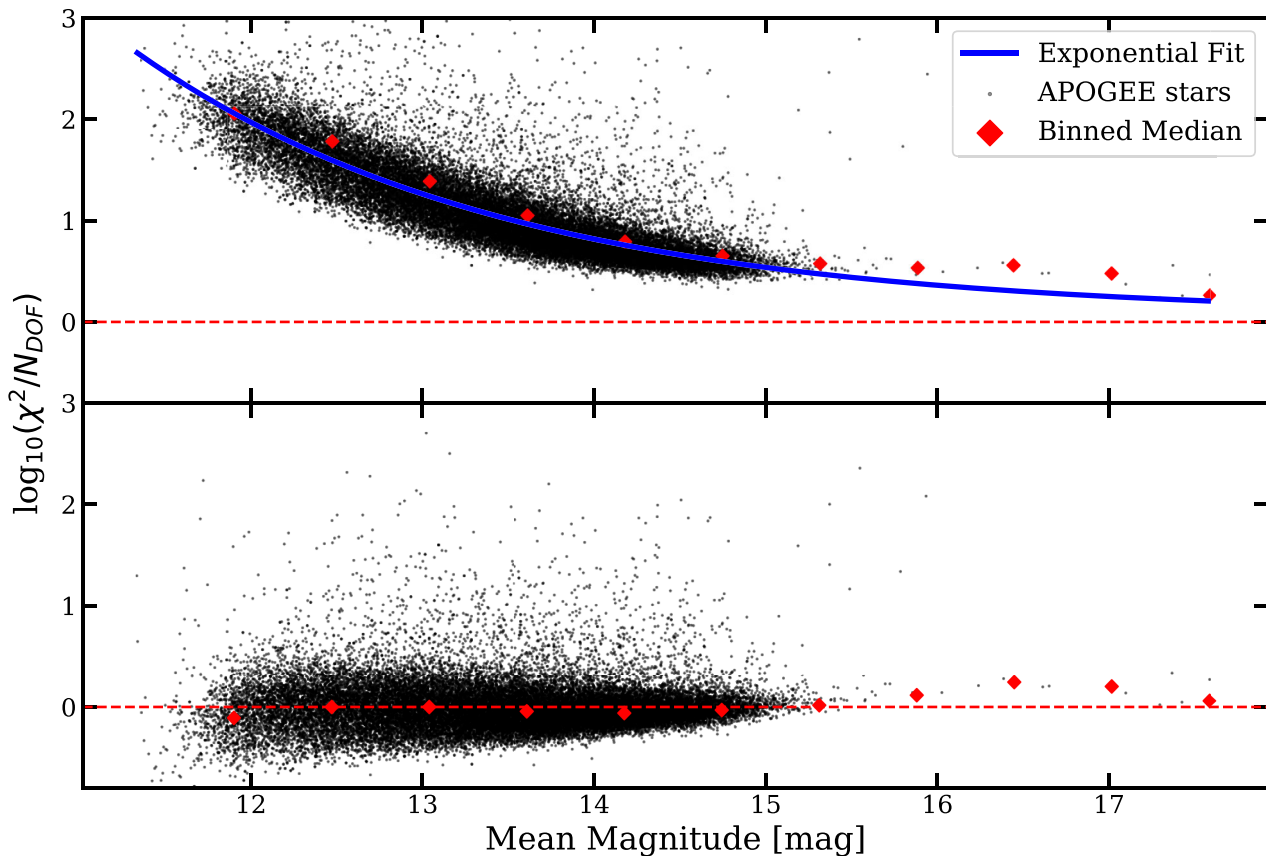
Figure 1. The top panel shows the raw distribution of $\log(\chi^2/N_{\rm dof})$ for the APOGEE stars prior to the rescaling process. The red dashed line illustrates the expected value of $\chi^2/N_{\rm dof} = 1$. The red points are the binned median values of $\log(\chi^2/N_{\rm dof})$ for this sample in bins of ~0.5 mag. The curve shows an exponential model (equation 2) of the trend and the bottom panels shows the distribution of $\chi^2/N_{\rm dof}$ after rescaling the errors.

3.2 Period determination

We used the Generalized Lomb-Scargle (GLS, Zechmeister & Kürster 2009; Scargle 1982), the Multi-Harmonic Analysis Of Variance (MHAOV, Schwarzenberg-Czerny 1996), the Phase Dispersion Minimization (PDM, Stellingwerf 1978), and the Box Least Squares (BLS, Kovács, Zucker & Mazeh 2002) periodograms to search for periodicity. We use the `astropy` implementation of the GLS algorithm (Astropy Collaboration et al. 2013), the `P4J` implementation of the MHAOV periodogram (Huijse et al. 2017), the `pwkit` implementation of the PDM periodogram (Williams et al. 2017), and the `astrobase` implementation of the BLS periodogram (Bhatti et al. 2018).

To minimize the effects of outliers when searching for periods, we only use the epochs with magnitudes between the 5th and 95th percentiles as input to the periodograms. We searched for periods in the range $0.05 \leq P \leq 1000$ d. The MHAOV periodogram was initialized with $N_{\rm harm} = 2$ harmonics. The BLS periodogram was initialized with 200 phase bins and a minimum (maximum) transit duration of 0.1 (0.3) in phase. For the GLS and MHAOV periodograms, periods were selected with S/N >5, while BLS periods were selected with the BLS power <0.3. Sources that do not have a single period based on these criteria are flagged as candidate irregular variables. The five best periods from each periodogram were passed to the PDM algorithm as test periods to minimize the dispersion of the light curve in 20 phase bins. The overall best period for each variable was defined to be the best PDM period.

During the first stage of our variability classification process, we utilized just the GLS, MHAOV, and PDM periodograms. From the visual review of these classifications, we noted that our pipeline was unable to retrieve periods for a large fraction of the detached (Algol-type) eclipsing binaries. This can be attributed to the non-sinusoidal shapes of the eclipses seen in these light curves. We used the BLS algorithm in the next stage of our classification process to solve this problem. Unlike the GLS and MHAOV algorithms, the BLS algorithm models a transit when searching for periods and is successfully able to derive periods for detached eclipsing binaries. Furthermore, Mira-like variability was best described by GLS periods, so we only used the GLS periodogram for variable sources with amplitudes $A > 2$ mag to minimize computational time.

In the case of eclipsing binaries, the periods returned by the periodograms are frequently a sub-harmonic of the true period, usually with $P = P_{\rm true}/2$. Armstrong et al. (2016) describes a possible remedy to this problem by comparing the difference between minima in phase folded K2 light curves. Periods are doubled when the minima are different by a user-defined constant. In the case of W UMa type contact binaries, the minima in the phase folded curve can be very similar, which is problematic for this method. Graham et al. (2013) suggests that the best approach to deal with the periods for eclipsing binaries is to simply double the period once it is confirmed that the light curve is that of an eclipsing binary.

We utilize a similar approach to that of Armstrong et al. (2016). Once a variable is classified as a candidate eclipsing binary, the
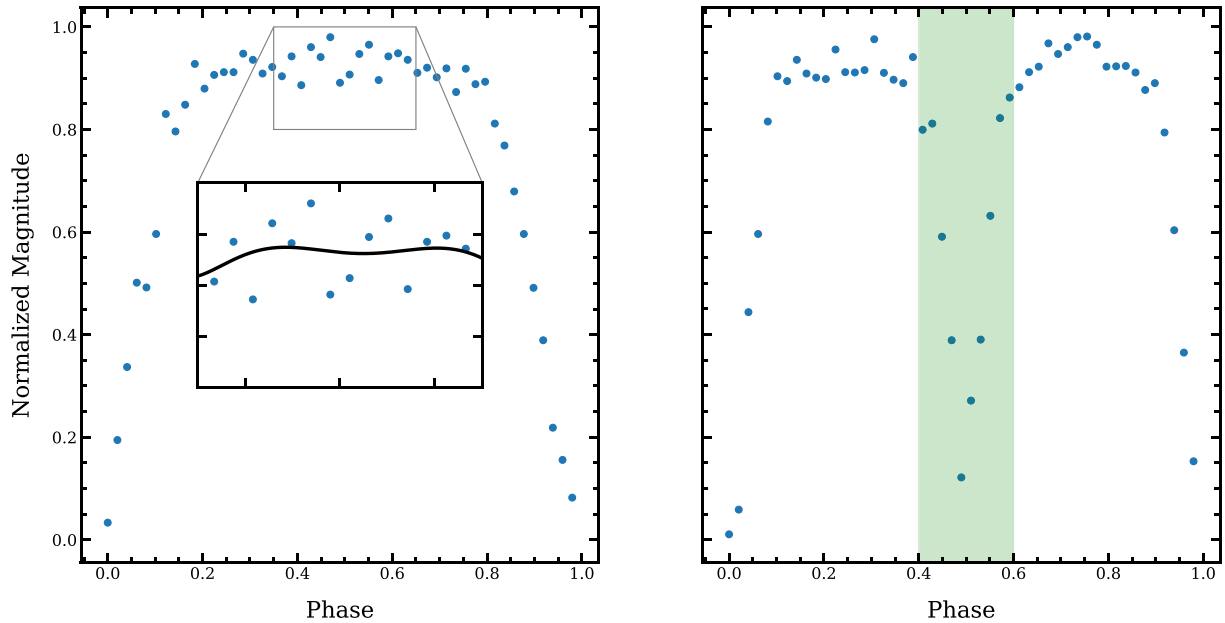
    T. Jayasinghe et al.

Figure 2. An illustration of the automated period doubling routine used on the ASAS-SN eclipsing binaries. Left: the original binned ($N_{bin} = 50$), phase-folded light curve for the detached eclipsing binary ASASSN-V J203611.47+003921.1 with $P = 0.25357$ d. The inset shows the region in phase space where the secondary minimum is expected to occur. The sixth-order polynomial fit used in the analysis is shown in black. Right: the final binned ($N_{bin} = 50$), phase-folded light curve with $P = 0.50713$ d. Note the emergence of a secondary minimum of different depth after the period is doubled.

normalized light curve is divided into 20 bins, phase folded by the best PDM period with the primary minimum at phase 0 and normalized by the global minimum and maximum. To search for the secondary minimum, we select all the points with phases in the interval [0.3,0.7], and fit a sixth-order polynomial to this data. If the global minimum of the polynomial is between phases 0.4 and 0.6, we consider the candidate period to be the true period. If the global minimum for the polynomial is beyond this range in phase space, we double the period. We find this method to be fairly robust, although it does fail in a limited number of cases where the light curves are noisy. This method could also fail for the light curves of eccentric binaries, and when the depth of the secondary minimum is comparable to the noise in the light curve. Fig. 2 illustrates this automated period doubling routine for the eclipsing binary candidate ASASSN-V J203611.47+003921.1.

3.3 Using the *Upsilon* classifier

For the first stage of our classification process, we used the open-source random forest classifier *Upsilon* (Kim & Bailer-Jones 2016). *Upsilon* is a general purpose random forest classifier trained using OGLE and EROS-2 data (Kim & Bailer-Jones 2016). For each ASAS-SN light curve, *Upsilon* calculates a set of features and provides a general variability classification. *Upsilon* also classifies certain variability classes into sub-classes (as an example, RR Lyrae are further classified as RRab, RRc, RRd, and RRe). We consider sub-classes for the RR Lyrae, Cepheid, and eclipsing binary classifications, but merge the other variability types with *Upsilon* sub-classes into a single class.

After classifying the ASAS-SN variable sources with *Upsilon*, we visually verified each classification. The RR Lyrae, Cepheids, and δ Scuti variables (DSCT) candidates were examined by at least two authors, while the remainder of the variability types were examined by only one author. Variables that pass the visual review at this stage are published in the catalogue and the remainder was

Table 1. Performance of the *Upsilon* classifier.

Class	Precision (per cent)
δ Scuti	68
RR Lyrae	83
Cepheids	10
Eclipsing binaries	63
Semiregular variables	36
Mira	75

saved for the next stage of the classification process. Through this process of visual review, we identified 22 809 periodic variables. To characterize these variables, we defined the amplitude A as the difference in the 2.5th and 97.5th percentiles in magnitude to mitigate the effects of outliers.

Variables were also tagged as 'variable/not irregular', 'variable/irregular', or 'bad' during the inspection process. Those tagged as 'variable/not irregular' were saved for the next stage of classification. Variables that were tagged as 'bad' generally had issues with photometry (bleeding trails, saturation, etc.) or astrometry (light curve extracted from the wrong position). These variables were removed from our working list. A further ∼37 000 candidates were tagged as 'variable/irregular' through this visual review.

Based on these reviews, we found that *Upsilon* achieves sufficient precision for well-defined variability types (e.g, RR Lyrae, Mira, eclipsing binaries, and δ Scuti) but fares poorly for other types (Table 1). The precision values in Table 1 were calculated as the ratio of the size of the positively reviewed sample to the size of the sample classified by *Upsilon* for any given variability type. Most of the false positives at this stage can be attributed to irregular variables with aliased periods and noisy data.

We aim to classify these variables according to the variability types defined by the VSX (Watson et al. 2006) and GCVS (Samus et al. 2017) catalogues. Most of the variability types defined in the *Upsilon* classifier do not strictly map on to a VSX/GCVS

Downloaded from https://academic.oup.com/mnras/article-abstract/477/3/3145/4961151 by Univerzita Karlova v Praze, Matematicko-fyzikalni fakulta user on 15 October 2018

Table 2. Sub-classes assigned to the irregular variables.

Class	Criteria
L	$J < 10$, $J - K_s > 1.1$, and $B - V > 1.5$
L:	$J < 10$, $J - K_s > 1.1$, and $B - V$ not available
YSO	$J > 10$ and $J - K_s < 1.1$
	$J > 10$, $J - K_s > 1.1$, and $B - V < 1.5$
GCAS	$J - H < 0.2$ and $B - V < 0.2$ + visual review
VAR	Remainder of the sample

Notes: J, H, and K_s are the 2MASS magnitudes, while the B and V magnitudes are from APASS.

type, therefore we changed the *Upsilon* classifications based on the VSX/GCVS definitions. *Upsilon* classifies eclipsing binaries into three types: EC (contact binaries), ESD (semi-contact binaries), and ED (detached binaries). EC classifications are changed to the 'EW' VSX type (W UMa type binaries), while the majority of the ESD classifications are assigned to the 'EA|EB' (Algol-type or β-Lyrae type) VSX class. Most variables classified as ESD with periods $P < 0.4$ d are EW types, and were reclassified accordingly. ED classifications were changed to the 'EA' VSX type (Algol-type binaries).

Cepheids are classified as fundamental mode, first overtone and type II Cepheids by *Upsilon*. We visually reviewed each classification to sort them into the VSX types DCEP (fundamental mode), DCEPS (first overtone), CWA/CWB (Type II: BL Herculis/W Virginis types), AHB1 ('Above Horizontal Branch' variables of sub-type 1), and ROT (rotational variables). Some ∼14 per cent of the variables classified as Cepheids by *Upsilon* are spotted variables showing evidence of rotational modulation. CWA and CWB variables are separated by period, with CWA (CWB) variables having $P > 8$ d ($P < 8$ d). AHB1 variables have highly asymmetric light curves with large amplitudes that resemble the light curves of RRab variables, allowing them to be separated from short-period fundamental-mode Cepheids (DCEP).

Upsilon assigns δ-Scuti variables to the DSCT class. We further categorize this class by selecting high-amplitude δ-Scuti (HADS) variables based on the amplitude cut $A > 0.15$ mag. Semiregular variables are assigned the VSX types of SR and SRS based on their period. SRS variables are short-period semiregular variables with $P < 30$ d, while semiregular SR variables have $P > 30$ d.

Mira variables (VSX type 'M') in our sample frequently dip below our detection limits ($V \gtrsim 17$), hence their ASAS-SN amplitudes can be less than the minimum V-band amplitude of $A = 2.5$ mag used by the VSX/GCVS catalogues to distinguish between high-amplitude semiregular variables and Miras. This can also lead to incorrect periods in a few cases where the light curve is inadequately sampled. We have visually reviewed the Miras to verify the shapes of their light curves and periods, but we caution that the true period might differ from what is reported in this catalogue.

To classify the ∼37 000 irregular variables, we utilize the 2MASS and APASS magnitudes following the criteria given in Table 2. The VSX classes 'L' and 'L:' are assigned to the irregulars with red $J - K_s/B - V$ colours and no infrared excess, while the VSX class 'YSO' (young stellar object) is assigned to the irregulars with faint infrared magnitudes ($J > 10$), intermediate to red colours, and an infrared excess. Blue irregulars with $J - H < 0.2$ and $B - V < 0.2$ are classified as Be stars in outburst (VSX class 'GCAS'). Candidates that met these criteria were visually reviewed to confirm the presence of outbursts. We were able to identify 79 GCAS candidates. The irregulars that do not fit into these classes

are assigned the generic 'VAR' (variable) class. These irregular variables were also added to the catalogue at this stage.

3.4 Random forest classification

Next we built our own classifier based on the ASAS-SN data using the `scikit-learn` (Pedregosa et al. 2012) implementation of the random forest classifier. We set the number of decision trees in the forest to be `n_estimators=700` and the number of features considered at each branching point to be `max_features='log2'`. The base 2 logarithm of the total features passed on to the random forest classifier is widely considered to be the optimal choice for this parameter. To prevent the forest from overfitting the data, we pruned the trees at a maximum depth of `max_depth=12`, set the number of samples needed to split a node to `min_samples_split=50` and set the number of samples at a leaf node to be `min_samples_leaf=10`. Our training sample consists of variables that passed the *Upsilon* classification and visual review process. There is a distinct imbalance of variables amongst the different classes. The irregular variables (∼10^4 sources) outnumber all the other variability types. The smallest classes, like the DCEP variables, consist of a meager ∼10^2 sources. An imbalanced training set can cause overfitting, hence we assign weights to each class in the training set by initializing `class_weight='balanced_subsample'`. These parameters were optimized using cross-validation.

In addition to tuning the random forest, one must choose the features of the data that may distinguish between the variable classes. We use a set of 16 features that have commonly been used in similar variability classification problems (see Pashchenko et al. 2018, and references therein). For the periodic variables, we fit a Fourier model,

$$M(\phi) = m_0 + \sum_{i=1}^{4} (a_i \sin(2\pi i\phi) + b_i \cos(2\pi i\phi)) \quad (3)$$

where m_0 is fixed as the median magnitude for each source and ϕ is the phase at a given epoch. The amplitude of the ith harmonic is given as $A_i = (a_i^2 + b_i^2)^{1/2}$ and the phase angle is $\Phi_i = \tan^{-1}(b_i/a_i)$. As variability features, we use the amplitude ratios of the harmonics defined as $R_{ij} = A_i/A_j$, the ratios of the Fourier components defined by $a_{ij} = a_i/a_j$ and $b_{ij} = b_i/b_j$, and the difference in phase angle between two harmonics defined by $\Phi_{ij} = \Phi_i - \Phi_j$. The complete list of features is summarized in Table 3.

3.4.1 Training and evaluating the classifier

We split the classified variables (*Upsilon* + visual review) into separate lists for training (80 per cent) and testing (20 per cent). To minimize class confusion, we merged variability types having many sub-classes into a single class. The final list of classes is: DSCT, CEPH, RRab, RRc, M, SR, IRR, EA, EA|EB, and EW. Variability types with <50 members (i.e. ROT, RRD, etc.) were dropped from both the training and test lists. We hope to revisit such classes at a later stage of the project where we supplement our training set with light curves for all the known, bright variables.

Fig. 3 highlights the feature importances derived from the trained random forest model. The period and colour provides the greatest discrimination between the variable sources, with a combined importance of 38.8 per cent. Several features (a_{42}, b_{42}, Φ_{42}, Φ_{31}, and K) do not discriminate significantly between the variables (importances $\lesssim 5$ per cent). Fig. 4 illustrates the random forest model's

Table 3. Variability features used to train the random forest classifier.

Feature	Description	Reference
$\log P$	Base 10 logarithm of the period	–
$J - H$	2MASS $J - H$ colour	Skrutskie et al. (2006)
A	Amplitude of the light curve	–
M_s	Skewness of the magnitude distribution	–
M_k	Kurtosis of the magnitude distribution	–
T_m	M-test statistic	Kinemuchi et al. (2006)
IQR	Difference between the 75th and 25th percentiles in magnitude	–
a_{42}	Ratio between the Fourier components a_4 and a_2	–
b_{42}	Ratio between the Fourier components b_4 and b_2	–
R_{31}	Ratio between the amplitudes of the third and first harmonics	–
R_{21}	Ratio between the amplitudes of the second and first harmonics	–
Φ_{42}	Difference between the phase angle of the fourth and second harmonics	–
Φ_{31}	Difference between the phase angle of the third and first harmonics	–
A_{HL}	Ratio of magnitudes brighter or fainter than the average	Kim & Bailer-Jones (2016)
rms	The rms statistic for the light curve	–
K	Stetson K variability index	Stetson (1996)
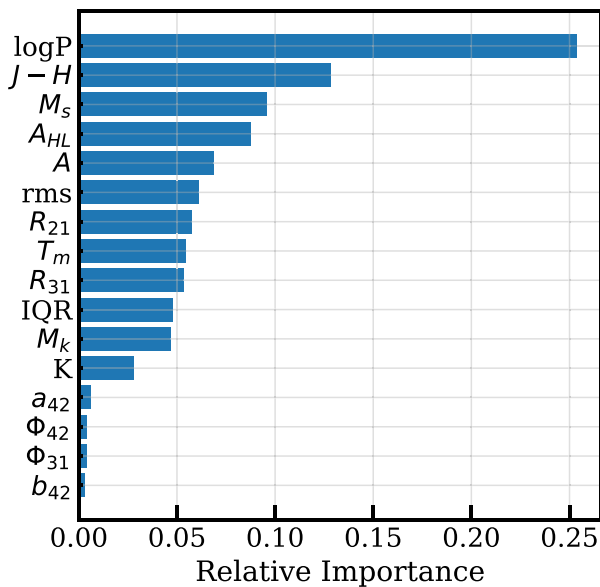
Figure 3. A bar chart illustrating the relative importance of the features listed in Table 3 that were used to train the random forest classifier.

ability to classify new objects. A perfect model would correctly classify all the objects, leading to a perfectly diagonal confusion matrix. Class confusion is greatest between the sub-classes of the eclipsing binaries, but this confusion does not significantly extend to mixing the eclipsing binaries with the non-binary classes. Semiregulars and irregulars are also frequently confused, which is to be expected given the somewhat hazy distinction between them.

We can evaluate the overall results based on the precision,

$$P = \frac{T_p}{T_p + F_p}, \qquad (4)$$

and recall,

$$R = \frac{T_p}{T_p + F_n}, \qquad (5)$$

where T_p and F_p (T_n and F_n) are the numbers of true and false positives (negatives). The precision and recall values for each class used in the random forest classifier are shown in Table 4. The over-

all precision and recall parameters of 89 per cent and 85 per cent, respectively were calculated using a weighted average.

The final random forest model was trained using the entire data set with the same initialization conditions as those used to test and verify the model. We used the trained random forest model to reclassify ∼6000 variable sources that were potentially misclassified by the *Upsilon* classifier and an additional ∼4000 new variable candidates identified in the interim. All the classifications were reviewed by at least a single author to ensure their accuracy and to verify the quality of the light curves before including these sources in the catalogue.

4 THE NEW VARIABLE STARS

The complete catalogue of 66 179 new variables is available at the ASAS-SN Variable Stars Database (https://asas-sn.osu.edu/variables) along with the *V*-band light curves for each source. Table 5 lists the number of sources of each variability type in the catalogue. This catalogue can be downloaded in its entirety at the ASAS-SN Variable Stars Database and is also included in the VSX catalogue of variables. This data base will continue to be updated as we discover new variables and reclassify existing ones. We intend to populate this data base with the light curves of all the known variables in our data over the next year. Our goal with the ASAS-SN Variable Stars Database is to provide a homogeneous set of light curves for all bright, known variable sources ($V \lesssim 17$ mag).

We note that the ASAS-SN catalogue is not complete – this was not an endeavor to do a statistically well-defined, all-sky search for variable stars, but rather a classification of variable sources that were flagged during our search for supernovae. Nevertheless, this catalogue is likely to contain a significant fraction of all previously undiscovered, high-amplitude variables at these magnitudes. High-amplitude variables are more likely to be flagged as variables during the search for supernovae, since these sources stand out from other low-amplitude variables in the difference images. The estimated variability amplitudes can be underestimated due to crowding and blending, particularly in the Galactic plane.

Fig. 5 shows the distribution of these new variables in mean brightness and amplitude (blue) as compared to the ∼370 000 other pulsating and eclipsing variables in the VSX catalogue with amplitudes $A > 0.05$ mag (red). The average variable in our catalogue has a mean brightness of $\overline{V} \sim 14.3$ mag and a mean amplitude
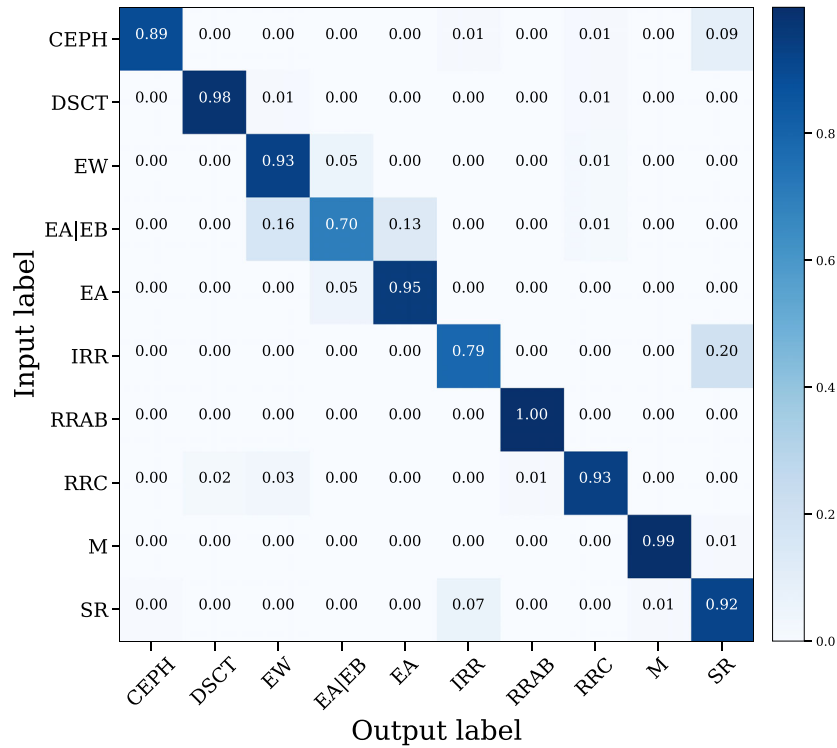
Figure 4. The normalized confusion matrix derived from the trained random forest classifier for the ASAS-SN variables. The *y*-axis corresponds to the 'input' classification given to a variable, while the *x*-axis represents the 'output' prediction obtained from the trained random forest model.

Table 4. Precision and recall values by class.

Class	Precision (per cent)	Recall (per cent)
EA	63	97
EA|EB	55	70
EW	93	93
δ Scuti	91	99
RRab	98	100
RRc	90	92
Cepheids	69	89
Mira	89	99
Semiregular variables	63	99
Irregular variables	97	79

of $A \sim 0.69$ mag. Fig. 6 shows the root mean square (rms) of the light curves as a function of their mean brightness. Not surprisingly, fainter variables tend to have higher amplitudes. The high-amplitude variables at bright magnitudes will have been found by shallower searches like ASAS. Our new catalogue increases the number of known variables with magnitude $13 < V < 16$ by~ 30 per cent, largely by filling in the lower amplitude variables missed by (presumably) shallower surveys.

To examine the distribution of these variables in 2MASS colour–colour and colour–period space, we grouped the variables into seven categories. Blue pulsators are the RR Lyrae, Cepheid (including type II Cepheids), δ Scuti, and AHB1 variables. Red pulsators are the Mira and semiregular variables. The irregular variables are the L, L:, and YSO sub-types. Eclipsing variables contain the EW, EA|EB, and EA classes. The GCAS, Rotational (ROT), and VAR categories directly map on to their respective VSX classes.

Fig. 7 shows the distribution in 2MASS colour ($J - H, H - K_s$) and period ($J - H$, P). There is a clear dichotomy between the red and blue pulsators in our sample. Most of the eclipsing systems are composed of blue, likely main-sequence stars. The generic VAR category mostly overlaps with the red pulsators, suggesting that a large fraction of these are actually red irregular variables. GCAS variables mostly occupy the lower left quadrant, while ROTs are scattered amongst the blue and red pulsators. The distinction between the different sub-types assigned to the ASAS-SN sample of irregulars in the 2MASS colour–colour space is shown in the middle panel.

Red pulsators have the largest periods and are clustered at the top right quadrant of the bottom panel. Sub-structure is evident in the distribution of the blue pulsators, highlighting the different classes of variables that comprise this group. The eclipsing binaries overlap the distribution of blue pulsators having similarly short periods. Eclipsing binaries span a large range of periods from relatively short periods (~ 0.2 d) to large periods ($\sim 10^4$ d). Long-period eclipsing binaries with periods $> 10^2$ d are rare in our sample.

Fig. 8 shows the spatial distribution of the ASAS-SN variables in Equatorial coordinates. Most of our new variables are just above or below the Galactic disc. Many surveys avoided lower Galactic latitudes (e.g. Drake et al. 2014) and the few surveys of the Galactic plane tended to cover only a few degrees in latitude (e.g. Haas et al. 2012; Hempel et al. 2014).

4.1 Pulsating variables

Our catalogue is largely (~ 95 per cent) composed of pulsating variables, and from the $\sim 61\,000$ pulsating variables discovered by ASAS-SN, ~ 37 per cent are periodic variables. Here, we discuss

Table 5. New ASAS-SN variables by type.

Class	Description	Number discovered
EA	Detached Algol-type binaries	1530
EA|EB	Algol-type or β Lyrae-type binaries	529
EW	W Ursae Majoris type binaries	2427
DSCT	δ Scuti type variables	22
HADS	High-amplitude δ Scuti type variables	548
RRAB	RR Lyrae variables with asymmetric light curves	4820
RRC	First overtone RR Lyrae variables	653
RRAB/BL	RRAB variables showing the Blazhko effect	40
RRC/BL	RRC variables showing the Blazhko effect	7
RRD	Double mode RR Lyrae variables	39
AHB1	Above horizontal branch sub-type 1 (XX Vir) Variables	24
DCEP	δ Cephei-type/classical Cepheid variables	160
DCEPS	First overtone Cepheid variables	84
CWA	W Virginis type variables with $P > 8$ d	22
CWB	W Virginis type variables with $P < 8$ d (BL Herculis variables)	44
RVA	RV Tauri variables (sub-type A)	3
M	Mira variables	1853
SRS	Short-period semiregular variables with $P < 30$ d	162
SR	Long-period semiregular variables with $P > 30$ d	13 844
L	Red irregular variables	18 768
L:	Irregular variables with missing $B - V$ colours	10 620
YSO	Young stellar objects	4215
GCAS	Rapidly rotating early type stars	93
ROT	Spotted variables with rotational modulation	662
VAR	Variable star of unspecified type	5010
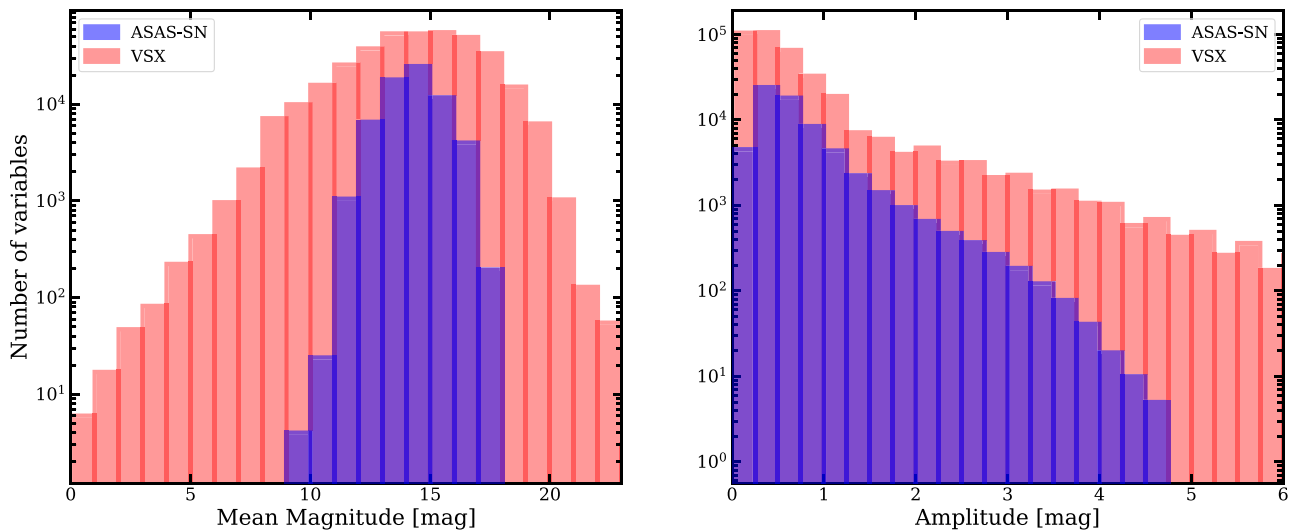
Figure 5. Histograms of the mean *V*-band magnitudes (left) and amplitudes (right) of the $\sim$66 000 new ASAS-SN variables (blue) as compared to the $\sim$370 000 known variables from the VSX catalogue (red) with amplitudes $A > 0.05$ mag. The average variable has a mean magnitude of $V \sim 14.3$ mag and mean amplitude of $A \sim 0.69$ mag.

the classes of pulsating variables in the ASAS-SN catalogue of variable stars and provide examples of the light curves for these classes of variables.

4.1.1 δ Scuti

δ Scuti stars are high-frequency pulsators (P<0.3 d) located at the lower end of the instability strip (Breger 1979). The δ Scuti variables are commonly sub-divided based on their amplitude. HADS have amplitudes ($A > 0.15$ mag) and are easily discovered by sky surveys similar to ASAS-SN. DSCT have amplitudes ($A < 0.15$ mag) and are

somewhat less commonly found due to the selection effect caused by their low amplitudes. This statement is reflected in the distribution of HADS/DSCT variables in our catalogue: $\sim$96 per cent are HADS variables. Examples of the DSCT and HADS classes are shown in Fig. 9.

4.1.2 RR Lyrae and AHB1/XX Vir variables

Jayasinghe et al. (2018) announced the discovery of 4880 RR Lyrae from the first stage of our variability classification process. Since then, we have discovered an additional 679 RR Lyrae in our data.
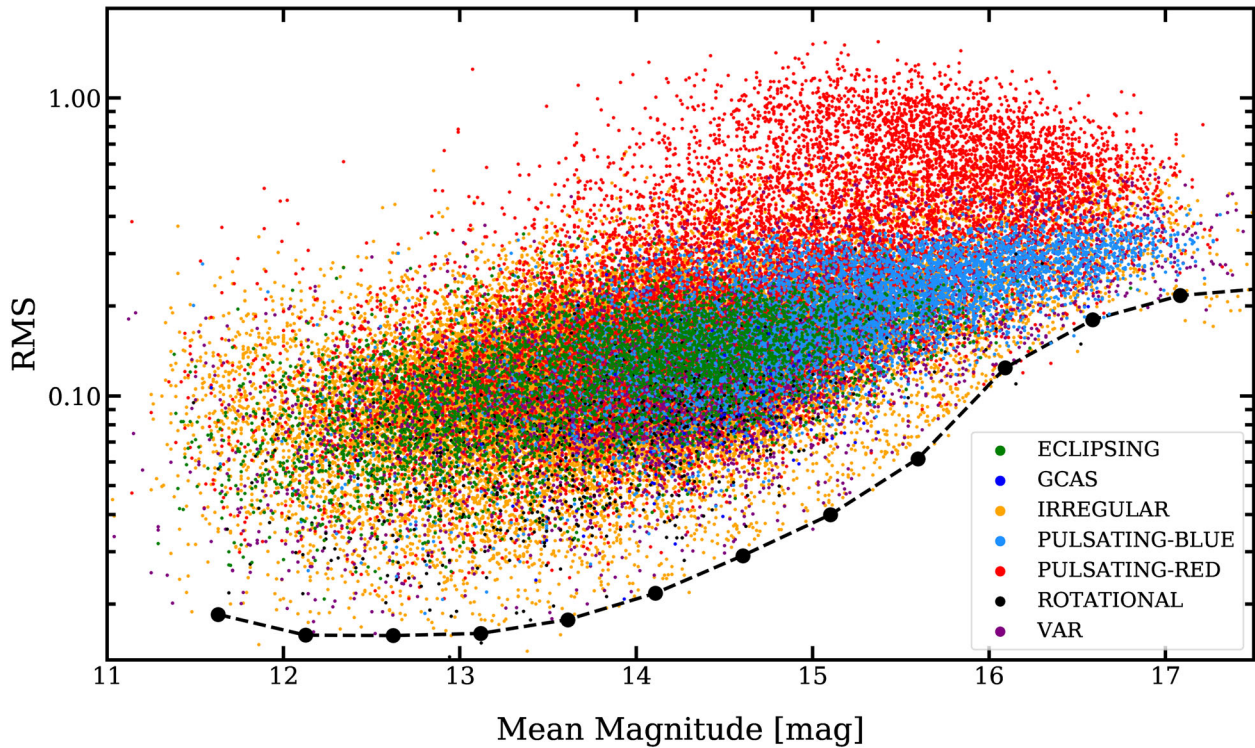
Figure 6. The rms variability as a function of mean magnitude for the new variable sources coloured by the variability groups described in the legend. The median rms of the APOGEE light curves used in Section 2.1 is shown in black.

Our catalogue of RR Lyrae stars largely consists of the RRAB (∼87 per cent) and RRC (∼12 per cent) types. A small fraction consists of double-mode RRD stars and RRAB/RRC stars showing the Blazhko effect (Blažko 1907).

A common issue that arises in the classification of RRC variables is cross-contamination with short-period contact binaries (EW). This is especially problematic for sources with amplitudes $0.3 < A < 0.5$ mag and periods $0.44 < P < 0.82$ d (Drake et al. 2014). In this parameter space, RRC variables can have almost symmetric light curves with morphologies similar to those of EW binaries phased with half their true period. EW binaries tend to have the light-curve skewness parameter $M_s > 0$, while most RRC variables have $M_s < 0$. One can potentially use this knowledge to reduce cross-contamination between these two variability types, but ultimately, one has to resort to spectroscopic follow-up to distinguish between these two variability types in the small number of cases where the light curves are photometrically ambiguous.

During the process of visual review, we identified 39 double-mode RR Lyrae candidates. Poleski (2014) studied double-mode radial pulsations amongst RR Lyrae stars and produced a Petersen diagram for RRD stars with the majority of their sample having $0.742 < P_{1O}/P_{FO} < 0.748$. Our RRD candidates were searched for secondary periods, and those with period ratios $0.73 < P_{1O}/P_{FO} < 0.77$ were classified as RRD stars. We chose this range in P_{1O}/P_{FO} to account for variations observed in RRD populations (Olech & Moskalik 2009) and parameter dispersions due to noise. The periods reported for the RRD stars are the best period derived for each light curve, where in most cases this is the period of the fundamental mode. We also identified 40 (7) RRAB (RRC) stars showing the Blazhko effect. These sources were classified based on the scatter around the primary maximum, which is indicative of the Blazhko effect.

AHB1 variables are evolved horizontal branch pulsators with periods $0.8 < P < 3$ d and asymmetric light curves resembling those of RRAB stars (Sandage & Tammann 2006). These variables are distinguished from low-period fundamental mode Cepheids by their low rise times to maximum and high visual amplitudes. We identify 24 candidate AHB1 variables.

Examples of the RR Lyrae and AHB1 classes are shown in Fig. 10.

4.1.3 Cepheids

Large numbers of these variables have been discovered over the years, since the first Cepheids were discovered in the Magellanic clouds by Leavitt (1908). For example, the current OGLE catalogue of Cepheids in the Magellanic Clouds boasts close to 10 000 Cepheids (Soszyński et al. 2017). In the Milky Way, only ∼1000 Cepheids are currently known (Windmark, Lindegren & Hobbs 2011). Fundamental-mode Cepheids (DCEP) are the archetypal classical Cepheids obeying a period–luminosity relation (Leavitt & Pickering 1912). DCEP variables have unique light-curve morphologies as a function of their period. First overtone Cepheids (DCEPS) have almost symmetrical light curves with periods $P < 7$ d and amplitudes $A < 0.5$ mag. We identified 160 fundamental mode and 84 first overtone Cepheids in our data. Over ∼80 per cent of the ASAS-SN DCEP and DCEPS variables are towards the Galactic disc.

Type II Cepheids overlap classical Cepheids in their periods but are intrinsically less luminous and have distinctive features in their light curves that separate them from classical Cepheids. Type II Cepheids also follow a period–luminosity relation (Matsunaga et al. 2006). BL Herculis type variables (CWB) have periods $P < 8$ d and have a unique bump along the descending branch in their phased light curves. W Virginis type variables (CWA) have periods $P > 8$ d
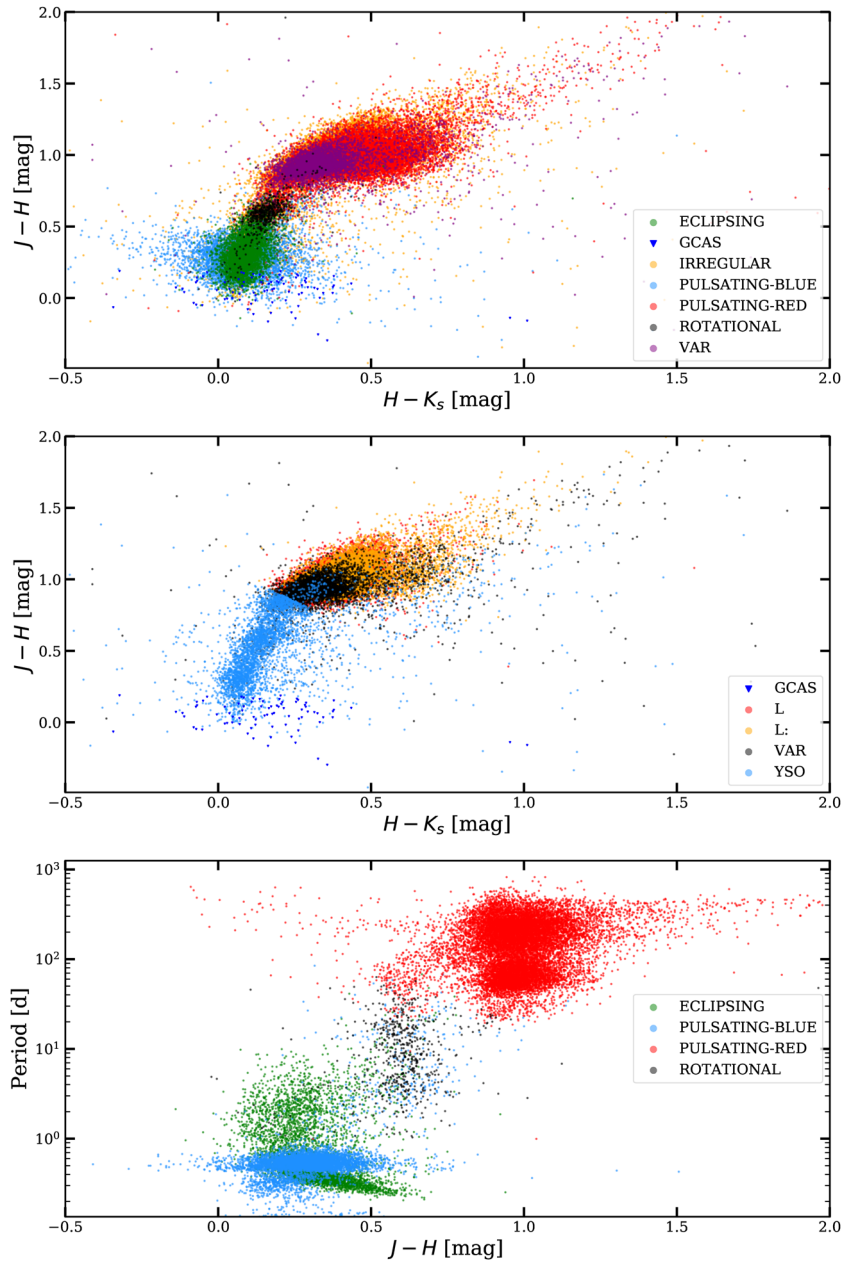
Figure 7. Top: the 2MASS colour–colour diagram for all the variables in our sample coloured by the variability groups described in the legend. Middle: the 2MASS colour–colour diagram for the irregular variables in our sample coloured by the variability groups described in the legend. Bottom: period–colour diagram for the periodic variables in our sample.

and light curves whose shapes are dependent on the period of pulsation. RV Tauri variables (RVA/RVB) have periods $30 < P < 150$ d and have alternating primary/secondary minima of different depths. The current sample contains 22 CWA, 44 CWB, and 3 RVA variables. We show examples of these variable types in Fig. 11.

4.1.4 Periodic red pulsators: Miras and semiregular variables

Mira variables (M) are asymptotic giant branch stars with high amplitude (typically defined as $A > 2.5$ mag in the V band) pulsations and periods $P > 100$ d. Mira variables can be further classified into sub-types based on the shapes of their light curves (Vardya 1988; Ludendorff 1928), and have also been found to follow a period–luminosity relationship (Whitelock, Feast & Van Leeuwen 2008). It

is not uncommon for Mira variables to show changes in their period (Percy & Colivas 1999). The current catalogue contains 1853 new Mira variables.

Semiregular variables are typically pulsating red giants with some periodicity in their light curves. These variables usually have irregularities in their light curves that distinguish them from other strictly periodic types, mostly due to multiperiodic behaviour (Kiss et al. 1999). We categorize our list of semiregular variables based on their period. Short-period semiregular variables (SRS) have periods $P < 30$ d, while SR variables have periods $P > 30$ d. It is likely that a number of the new semiregular variables are actually OGLE small-amplitude variable red giants (Soszynski et al. 2004) that follow a set of period–luminosity relations proposed by Soszynski et al. (2007). We note that the number of semiregular variables
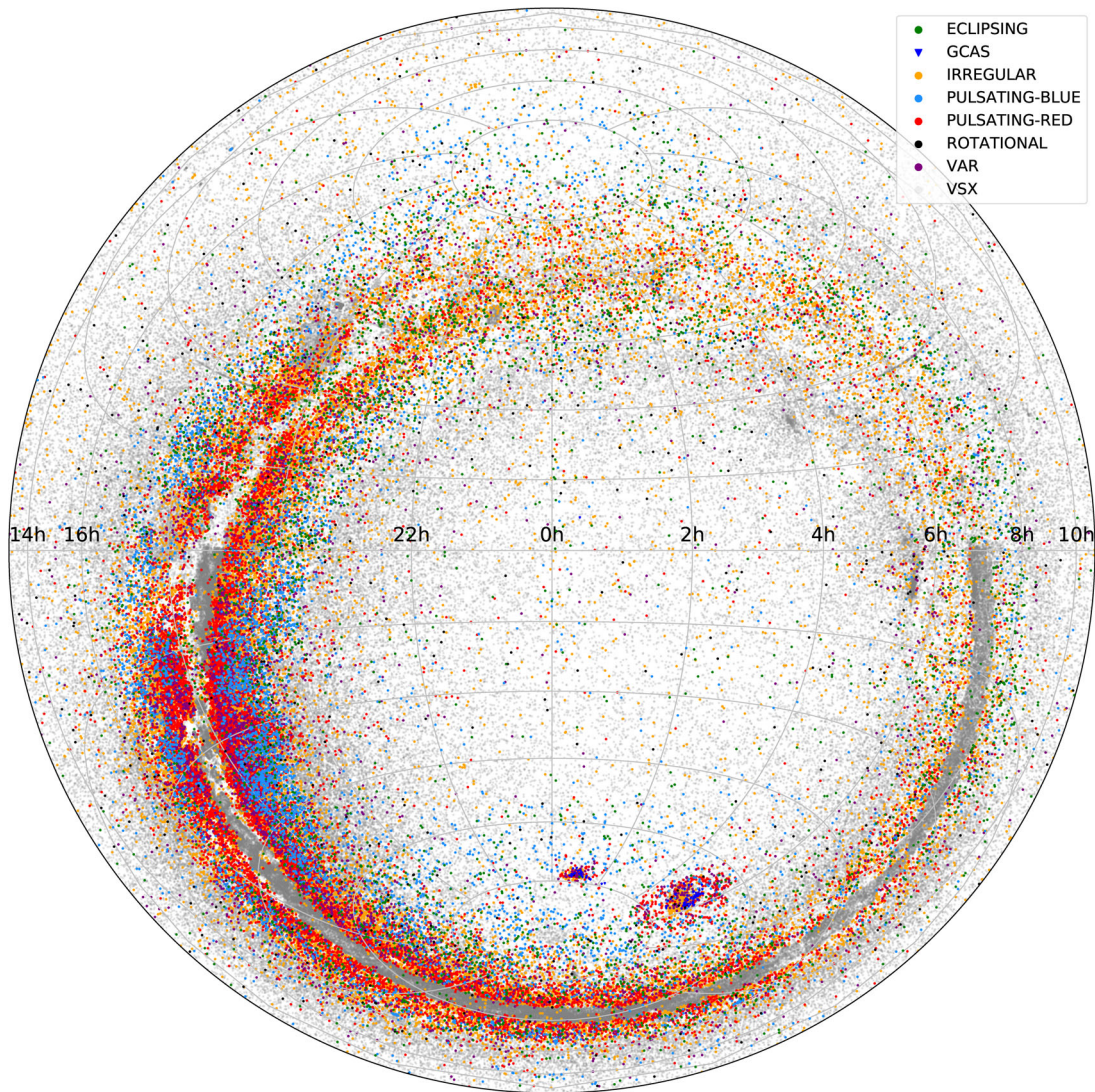
Figure 8. Spatial distribution of the ∼66 000 new ASAS-SN variables in equatorial coordinates. Grey points denote the ∼370 000 known variables from the VSX catalogue with $V < 17$ mag and $A > 0.05$ mag.

discovered by ASAS-SN (14 006) is ∼30 per cent of the total number of semiregular variables in the VSX catalogue.

Examples of Mira, SRS, and SR variables are shown in Fig. 12.

4.1.5 Irregular variables

Our catalogue contains several different sub-types of irregulars separated by their colours (see Section 3.3 and Table 2 for our classification criteria). The majority (∼75 per cent, see Table 5) are red irregulars (L/L:). This catalogue increases the number of red irregular variables in the VSX catalogue by ∼70 per cent. Irregulars with an infrared excess are classified as YSO. Examples of irregular variables are shown in Fig. 13.

4.2 Eclipsing binaries

Eclipsing binaries provide fundamental physical characteristics for stellar systems (see Torres et al. 2010, and references therein). These systems have been successfully used to derive masses and radii of stars in binary systems to a few per cent (Torres et al. 2010).

Recently, eclipsing binaries have also been used to derive extragalactic distances. For example, Pietrzyński et al. (2013) derived a ∼2 per cent distance to the Large Magellan cloud using a set of eight detached eclipsing binaries.

Photometrically, the light curves of eclipsing binaries are categorized into the GCVS/VSX classes: EW, EB, and EA. EW (W UMa) type systems have light curves with minima of similar depths and transition smoothly from the eclipse to the out-of-eclipse phase. EB (β-Lyrae) type systems also possess light curves that transition smoothly between these states, but have minima of significantly different depths. EA (Algol) type systems may not have a secondary minimum. It is relatively straightforward to pinpoint the exact onset and end of the eclipses in an EA system.

These classes correspond to the contact, semidetached, and detached binary configurations. Pojmanski (2002) classified the eclipsing binaries in the ASAS sample based on the likely physical configuration of the binary. While this makes sense probabilistically, the distinction between the different physical classes becomes ambiguous as the amplitude/depth of the eclipses decrease (Paczyński et al. 2006). Classifying eclipsing binaries into photometric classes
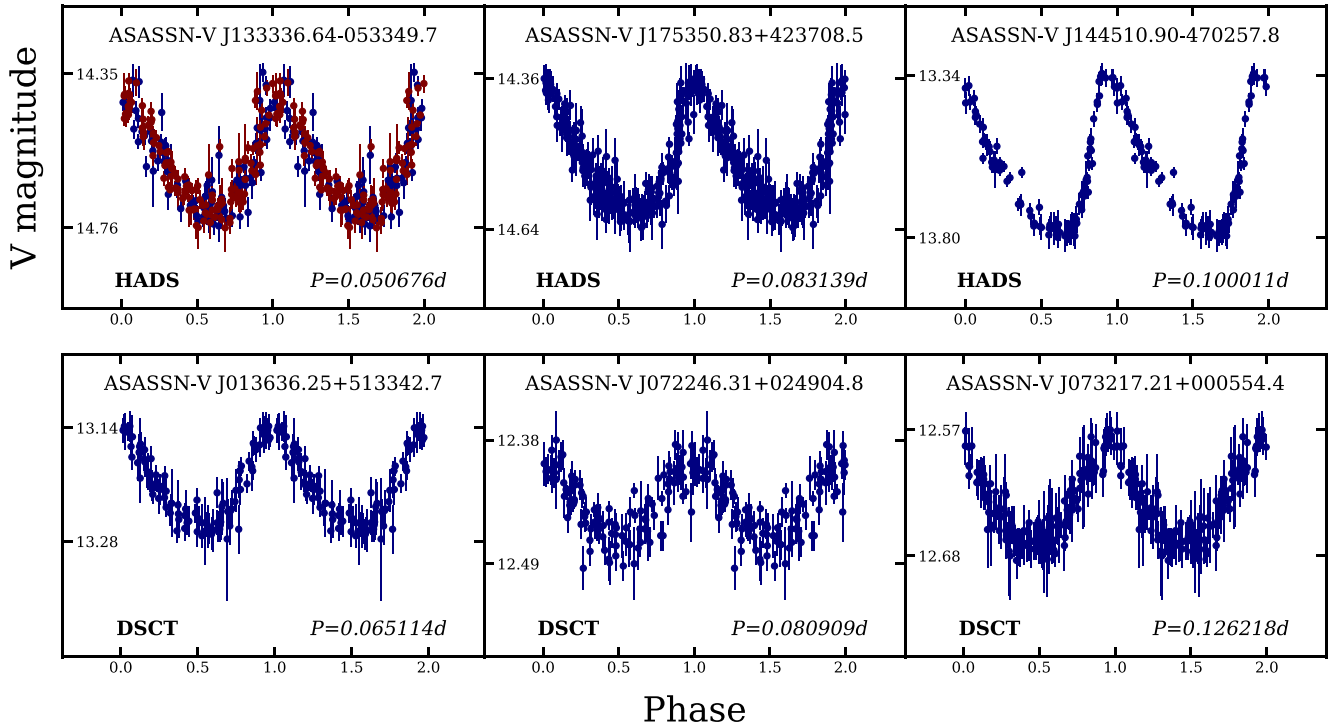
Figure 9. Phased light curves for examples of the DSCT and HADS VSX classes. The light curves are scaled by their minimum and maximum *V*-band magnitudes with different variable classes in each row. Different coloured points correspond to data from the different ASAS-SN cameras.

is more intuitive, but has its own problems. For example, it is sometimes difficult to distinguish between the EA and EB classes based on the light curve, so we grouped these sources into a joint class 'EA|EB' to improve our classifications. Based on our visual inspections, most of the binaries classified as EA|EB are actually EB types.

EW-type contact binaries typically have a lower limit to their periods of $P > 0.22$ d (Rucinski 1992). We find three EW binaries with ultrashort periods, ASASSN−V J024528.69−660648.0 (P=0.20644d), ASASSN-V J090523.70−284645.0 (P=0.20930d), and ASASSN-V J194752.88+725431.1 (P=0.21131d), and these are shown in Fig. 14. The VSX catalogue lists >350 EW binaries with periods $P < 0.22$ d, thus it is likely that the lower limit for EW periods are shorter than the limit imposed here.

We identify 207 short-period ($P < 1$ d) detached binaries. Recent evidence suggests that most short-period contact binaries are triple systems with tertiary companions (see Rucinski, Pribulla & van Kerkwijk 2007, and references therein). The Lidov–Kozai mechanism (Lidov 1962; Kozai 1962) is likely to have created these systems from short-period detached binaries (Mazeh & Shaham 1979; Kiseleva, Eggleton & Mikkola 1998; Eggleton & Kiseleva-Eggleton 2001; Paczyński et al. 2006; Eggleton 2012). We identified 2427 EW binaries, 529 EA|EB binaries, and 1530 EA binaries in our data. The eclipsing binaries in our sample span a range of periods from $0.20 < P < 68.0$ d. Examples of the EA|EB and EA classes are shown in Fig. 15.

4.3 Rotational variables

Light curves showing evidence of rotational modulation were classified as a generic rotational variable (ROT). We report the best period derived for each light curve and note that this may not be the actual period of rotation for the star. This class is likely to contain

numerous RS Canum Venaticorum-type (RS) binary systems along with BY Draconis-type variables and spotted T Tauri stars showing periodic variability. We identified 662 new ROT variables with examples shown in Fig. 16.

Jayasinghe et al. (2017e) recently reported the discovery of a likely extreme spotted variable ASASSN-V J211256.97+313724.6. This source had a period of $P = 5.412$ d and displayed amplitude modulation from $A = 0.58$ mag in 2014 to $A = 0.16$ mag in 2014. ASAS data also showed evidence of high-amplitude variability, suggesting an extreme degree of star spot coverage, persisting for ∼10 yr. Based on these lines of evidence, ASASSN-V J211256.97+313724.6 is most likely an RS binary system. Similar variables are likely to be found in our overall sample of 662 ROT variables.

4.4 GCAS variables

The VSX catalogue defines GCAS variables to be eruptive irregular variables of early spectral types (O9-A0 III-Ve) with mass outflow from their equatorial zones (Watson et al. 2006). A GCAS variable, ASASSN-V J010932.93+614659.0, was identified based on its light-curve morphology during the early stages of the variability classification process by Jayasinghe et al. (2017c). A low-resolution spectrum of this object taken with the MDM 2.4 m telescope and OSMOS spectrometer showed Balmer and He I lines in absorption, with a strong narrow-Hα profile in emission. These features are characteristic of a Be (GCAS) star. Subsequently, Steele (2017) obtained a medium-resolution spectrum with the FRODOSpec spectrograph on the Liverpool Telescope, deriving a spectral type of B6V and confirming that this source is a rapid rotator.

We identified 93 other GCAS variables in our data based on the criteria described in Section 3.3. The locations of these GCAS variables in the 2MASS colour–colour diagram are highlighted in
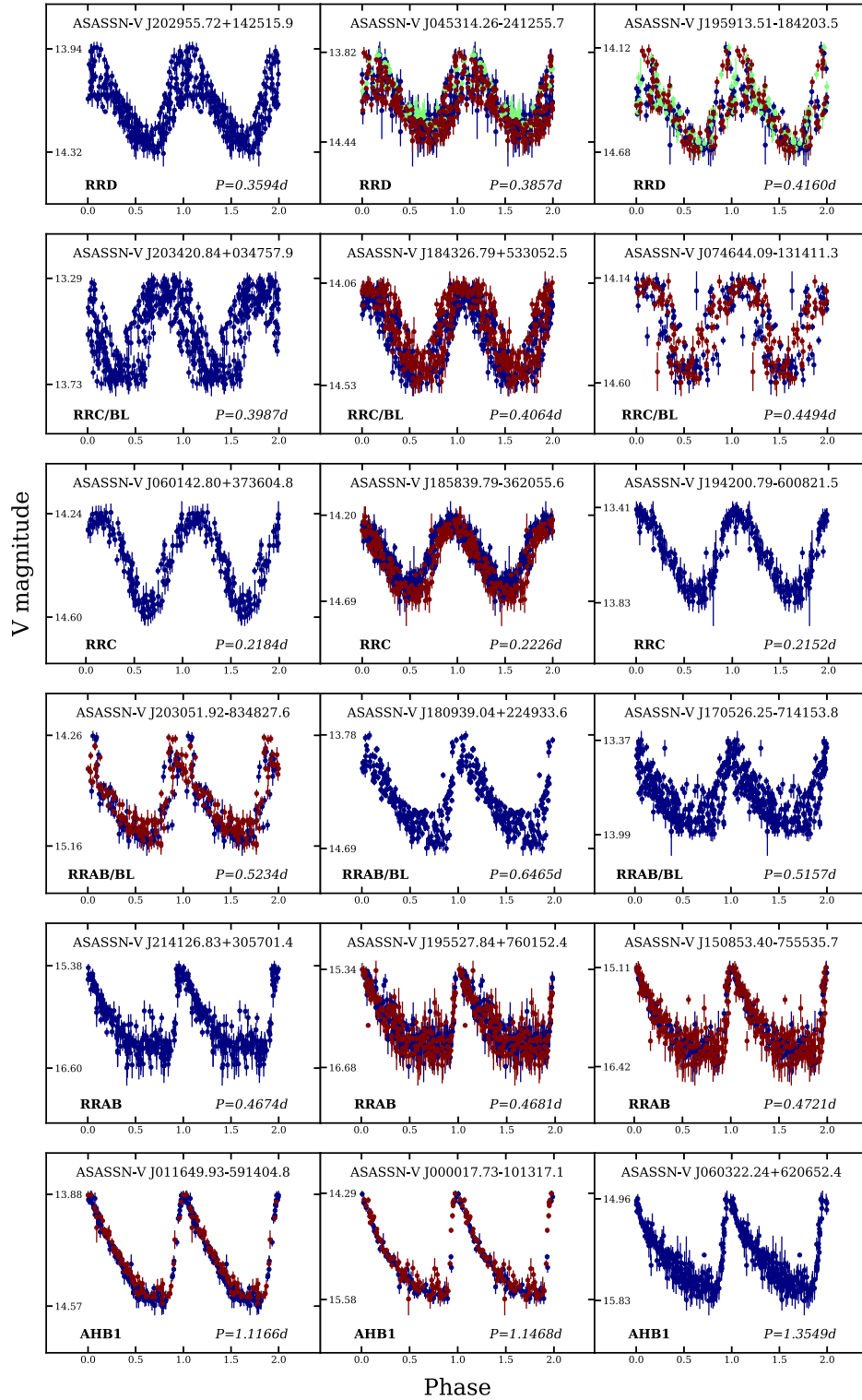
Figure 10. Phased light curves for examples of the RR Lyrae and AHB1 classes. The format is the same as for Fig. 9.

Fig. 8. Each of these sources were visually reviewed to identify outbursts similar to ASASSN-V J010932.93+614659.0 and other Be star outbursts (Labadie-Bartz et al. 2018). Based on our selection criteria, it is very likely that most of these sources are rapidly rotating early-type stars. Examples are shown in Fig. 17.

4.5 Microlensing events

We discovered two bright, archival microlensing events in our data (Jayasinghe et al. 2017b, 2017d) during the variability classification process (Fig. 18). ASASSN-V J182456.34−305816.7 was discovered near the Galactic bulge with a peak magnification of 16,
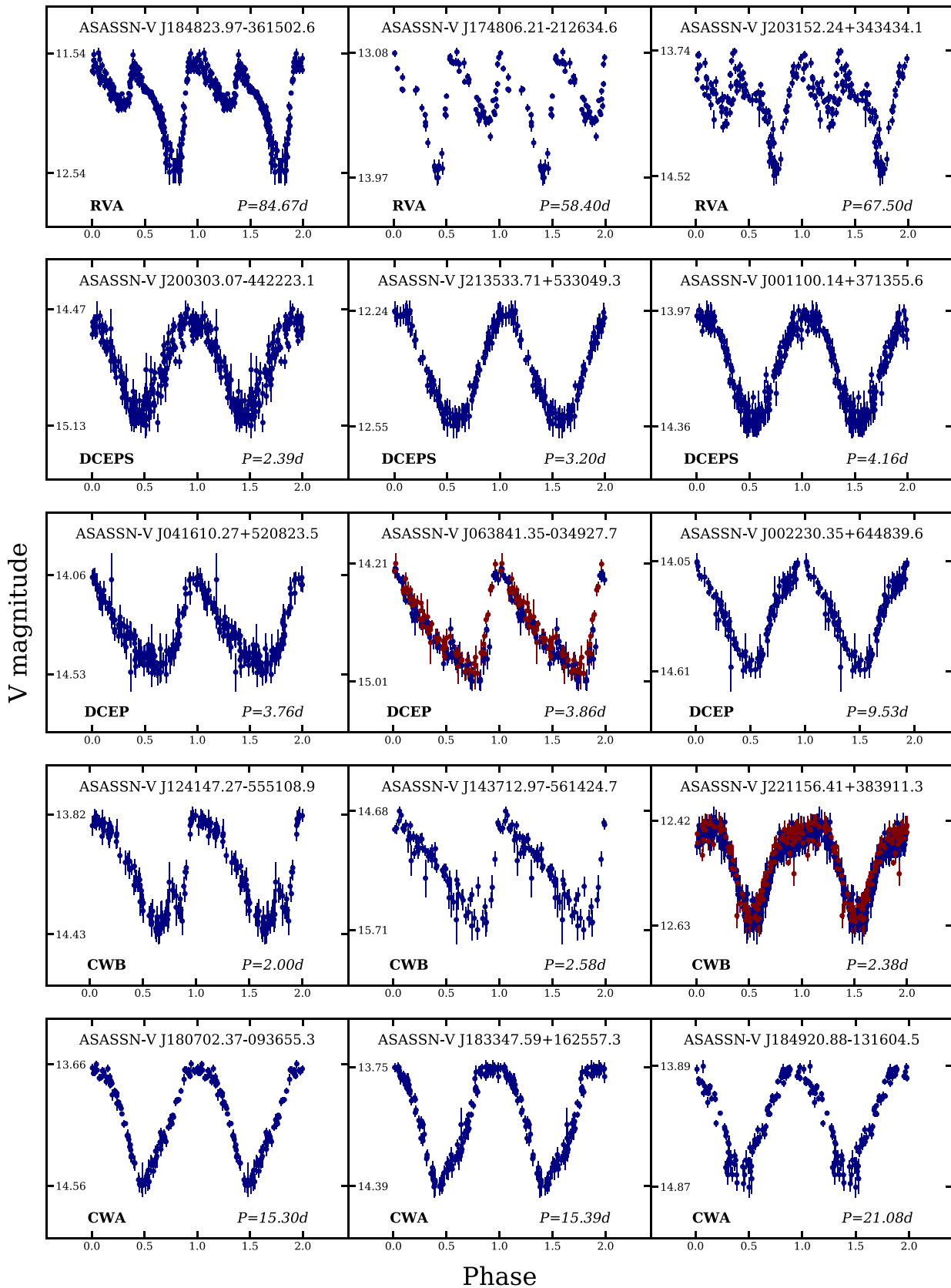
Figure 11. Examples of the DCEP, DCEPS, CWA, CWB, and RVA VSX classes. The format is the same as for Fig. 9.
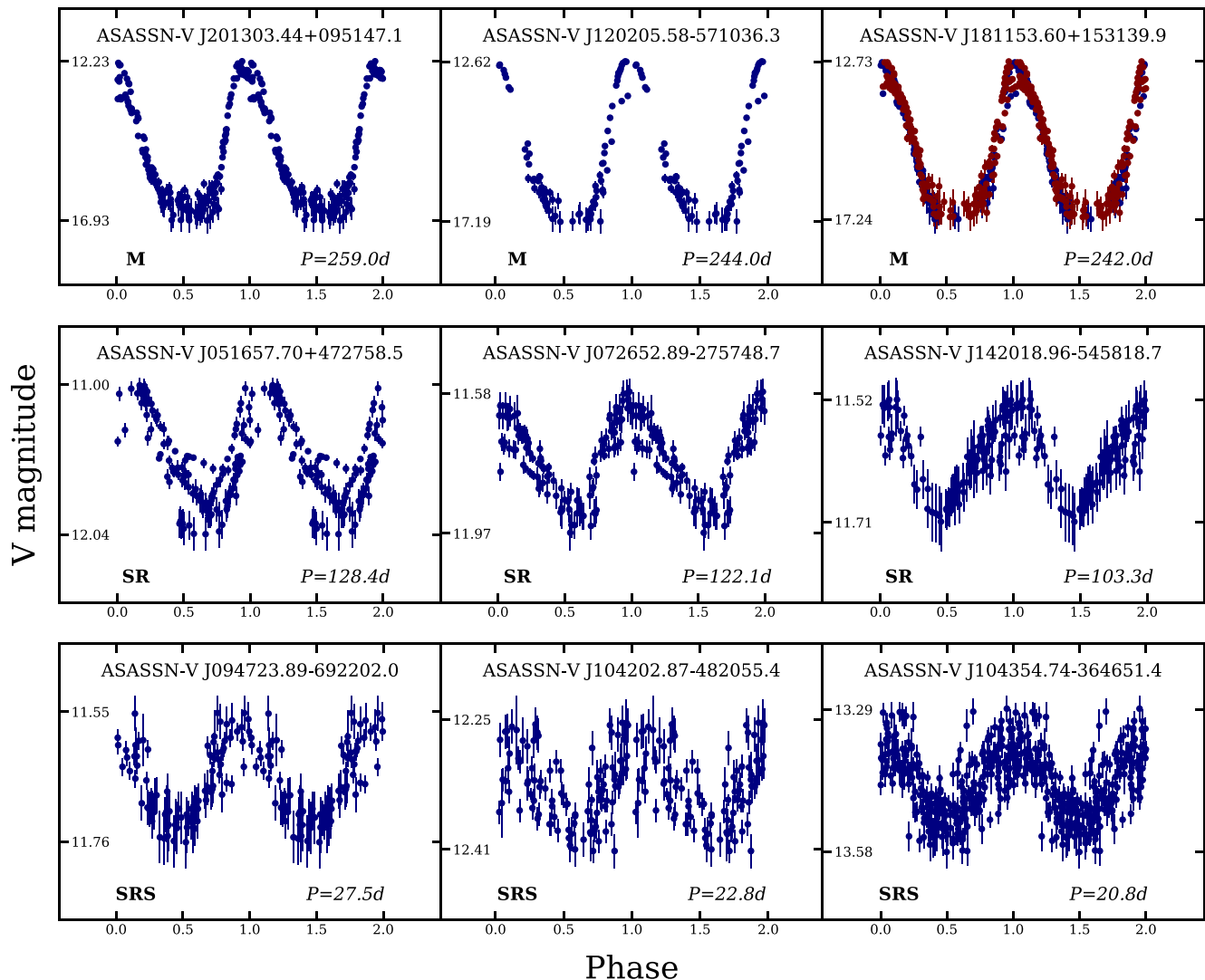
Figure 12. Examples of the periodic red pulsators in our sample, which include the SRS, SR, and M VSX classes. The format is the same as for Fig. 9.

and ASASSN-V J044558.57+081444.6 was discovered close to the Galactic anticentre with a peak magnification of 33. It is likely that more archival microlensing events are hidden within our data. We are currently conducting a systematic search of the irregular variables to find additional archival microlensing events.

4.6 Other discoveries

Jayasinghe et al. (2017a) discovered two variables: ASASSN-V J033455.88−053957.9 and ASASSN-V J211014.40−242105.3, with unusual light curves (Fig. 19). ASASSN-V J033455.88−053957.9 is a probable early-type M-dwarf that brightened by 0.5 mag over a period of ∼1800 d. It appears in a number of X-ray catalogues, including the Swift X-ray point source catalogue (Evans et al. 2014). The light-curve characteristics of this source are atypical of an M-dwarf.

ASASSN-V J211014.40−242105.3 was spectroscopically classified as a cataclysmic variable (CV) by Kilkenny et al. (2015). We found a fading event lasting at least 150 d in the ASAS-SN light curve. This fading event is a probable result of episodic mass transfer from the companion star (Leach et al. 1999), suggesting that

ASASSN-V J211014.40−242105.3 is likely a CV of the VY Scl type.

5 CONCLUSIONS

In this paper, we provide a catalogue of new variable stars identified by ASAS-SN during our search for supernovae. We classified the variables by:

(i) Cross-matching our list of sources with existing variable star catalogues to remove known variable sources;

(ii) Using an open source random forest classifier *Upsilon* (Kim & Bailer-Jones 2016) to derive initial classifications for our list of variable sources;

(iii) Visually reviewing the *Upsilon* classifications to select a sample of accurately classified variables while flagging irregular variables and removing bad sources;

(iv) Training a random forest classifier using the ASAS-SN data and their classifications; and

(v) Reclassifying all the sources along with any new variable sources discovered in the interim.
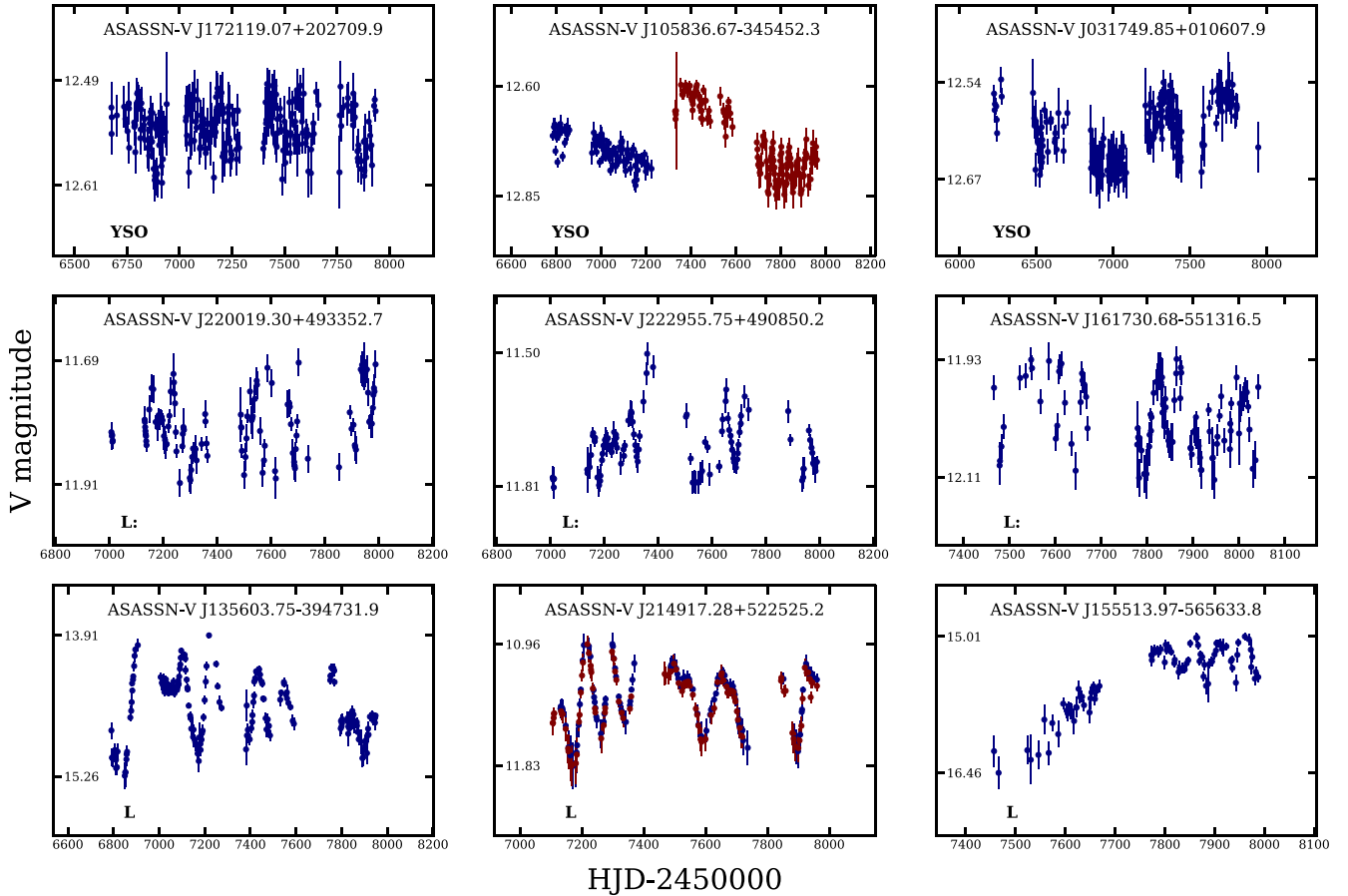
Figure 13. Examples of the irregular variables in our catalogue. The format is the same as for Fig. 9.
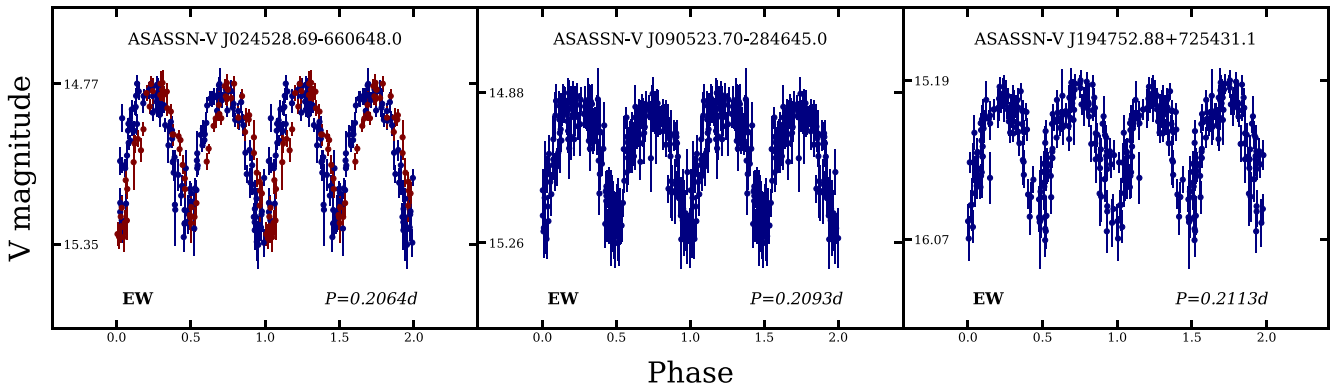
Figure 14. Phased light curves for the three ultrashort-period contact binaries in the catalogue. The format is the same as for Fig. 9.

The resulting catalogue of 66 179 bright ($V \lesssim 17$ mag) new variables is dominated by red pulsators ($\gtrsim 50$ per cent of the catalogue) and makes significant contributions to the current list of known semiregular and irregular variables. We also provide lists of common variables (RR Lyrae, eclipsing binaries, Cepheids, Miras, etc.) sampled over the whole sky. While this catalogue is not complete for low-amplitude variability, it goes a long way towards providing a largely complete sample of high-amplitude variables (including Miras and high-amplitude semiregular variables) down to $V \lesssim 16$ mag. We estimate the classification errors in this catalogue to be

$\lesssim 10$ per cent, with the majority of the errors resulting from confusion between similar variable classes (e.g. sub-classes of eclipsing binaries).

The complete list of ASAS-SN variables along with their *V*-band light curves are provided online at the ASAS-SN Variable Stars Database (https://asas-sn.osu.edu/variables). Light curves for bright, known variables will be added to this data base over the next year. The next step in our search for variable stars is to extract light curves for all ∼50 million APASS stars to carry out a systematic search.
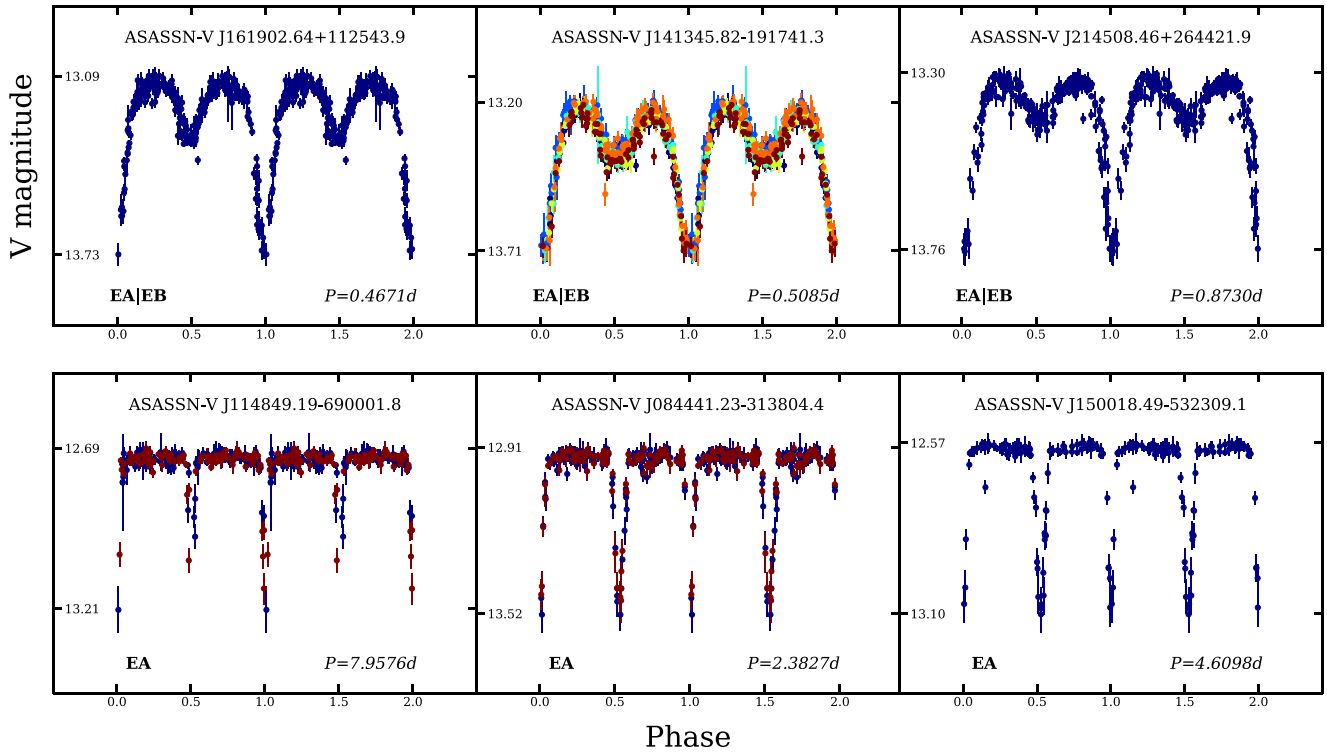
Figure 15. Examples of the EA|EB and EA classes. The format is the same as for Fig. 9.
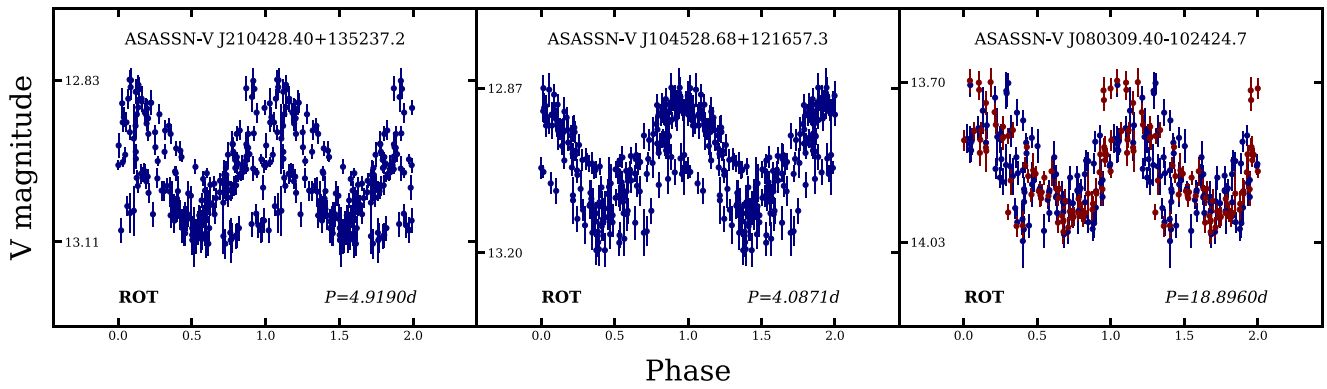
Figure 16. Examples of the ROT class. The format is the same as for Fig. 9.
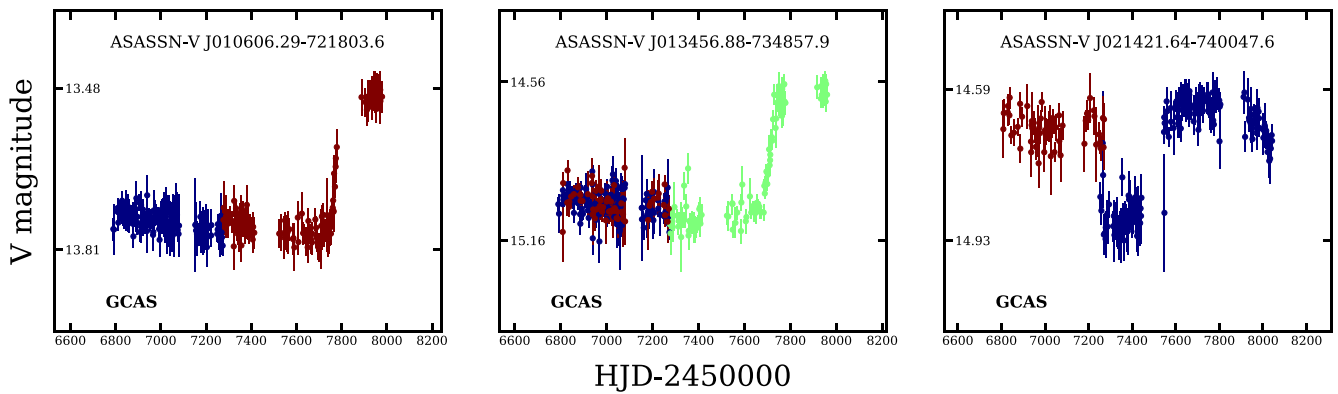
Figure 17. Examples of the GCAS variables. The format is the same as for Fig. 9.
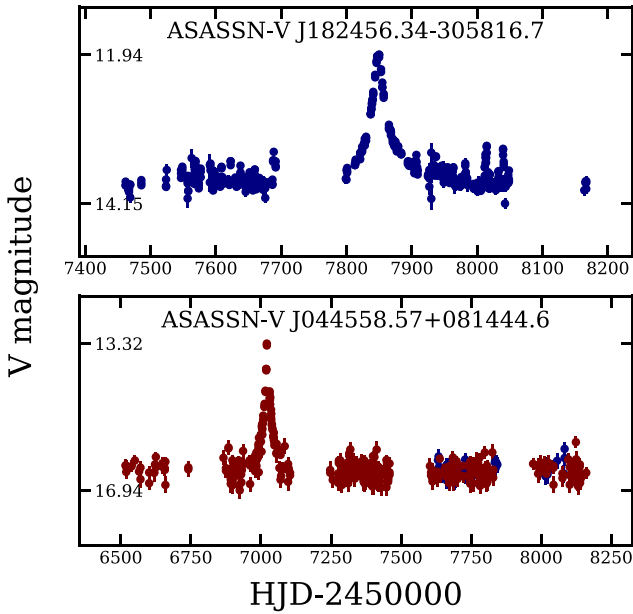
Figure 18. Light curves for the microlensing events ASASSN-V J182456.34−305816.7 and ASASSN-V J044558.57+081444.6. The format is the same as for Fig. 9.
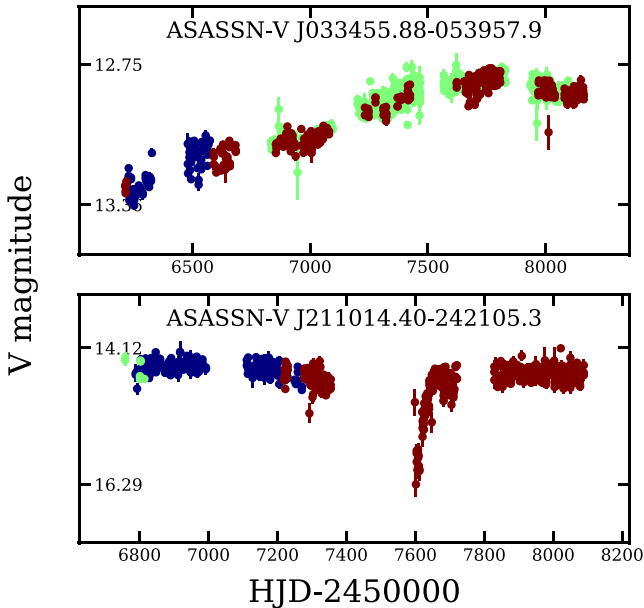

Figure 19. Light curves for the unusual sources ASASSN-V J033455.88−053957.9 and ASASSN-V J211014.40−242105.3. The format is the same as for Fig. 9.

ACKNOWLEDGEMENTS

REFERENCES

Alard C., 2000, A&AS, 144, 363
Alard C., Lupton R. H., 1998, ApJ, 503, 325
Alcock C. et al., 1997, ApJ, 486, 697
Armstrong D. J. et al., 2016, MNRAS, 456, 2260
Astropy Collaboration, 2013, A&A, 558, A33
Bhatti W. et al., 2018, Astrobase, v0.3.8, Zenodo, doi:10.5281/zenodo.1185231
Blažko S., 1907, Astron. Nachr., 175, 325
Breger M., 1979, PASP, 91, 5
Brown T. M. et al., 2013, PASP, 125, 1031
Chambers K. C. et al., 2016, preprint (arXiv:1612.05560)
Derue F. et al., 2002, A&A, 389, 149
Drake A. J. et al., 2014, ApJS, 213, 9
Eggleton P. P., 2012, J. Astron. Space Sci., 29, 145
Eggleton P. P., Kiseleva-Eggleton L., 2001, ApJ, 562, 1012
Evans P. A. et al., 2014, ApJS, 210, 8
Graham M. J., Drake A. J., Djorgovski S. G., Mahabal A. A., Donalek C., Duan V., Maker A., 2013, MNRAS, 434, 3423
Haas M., Hackstein M., Ramolla M., Drass H., Watermann R., Lemke R., Lemke R., 2012, Astron. Nachr., 333, 706
Hartman J. D., Bakos G., Stanek K. Z., Noyes R. W., 2004, AJ, 128, 1761
Hempel M., 2014, The Messenger, 155, 24
Henden A. A., Levine S., Terrell D., Welch D. L., 2015, American Astronomical Society Meeting Abstracts #225, 225, 336.16
Holoien T. W.-S., 2017, MNRAS, 471, 4966
Holtzman J. A., 2015, AJ, 150, 148
Huijse P. et al., 2017, ApJ, preprint (arXiv:1709.03541)
Jayasinghe T. et al., 2017a, Astron. Telegram, 10634
Jayasinghe T. et al., 2017b, Astron. Telegram, 10677
Jayasinghe T. et al., 2017c, Astron. Telegram, 10710
Jayasinghe T. et al., 2017d, Astron. Telegram, 10740
Jayasinghe T. et al., 2017e, Astron. Telegram, 11034
Jayasinghe T. et al., 2018, Res. Notes Am. Astron. Soc., 2, 18
Kilkenny D., O'Donoghue D., Worters H. L., Koen C., Hambly N., MacGillivray H., 2015, MNRAS, 453, 1879
Kim D.-W., Bailer-Jones C. A. L., 2016, A&A, 587, A18
Kinemuchi K., Smith H. A., Woźniak P. R., McKay T. A., ROTSE Collaboration, 2006, AJ, 132, 1202
Kiseleva L. G., Eggleton P. P., Mikkola S., 1998, MNRAS, 300, 292

Kiss L. L., Szatmáry K., Cadmus R. R., Jr, Mattei J. A., 1999, A&A, 346, 542

Kochanek C. S. et al., 2017, PASP, 129, 104502

Kovács G., Zucker S., Mazeh T., 2002, A&A, 391, 369

Kozai Y., 1962, AJ, 67, 591

Labadie-Bartz J., 2018, AJ, 155, 53

Law N. M., 2009, PASP, 121, 1395

Leach R., Hessman F. V., King A. R., Stehle R., Mattei J., 1999, MNRAS, 305, 225

Leavitt H. S., 1908, Ann. Harvard College Obs., 60, 87

Leavitt H. S., Pickering E. C., 1904, Harvard College Obs. Circ., 90, 1

Leavitt H. S., Pickering E. C., 1912, Harvard College Obs. Circ., 173, 1

Lidov M. L., 1962, Planet. Space Sci., 9, 719

Ludendorff H., 1928, Hand. Astrophys., 6, 49

Matsunaga N., 2006, MNRAS, 370, 1979

Mazeh T., Shaham J., 1979, A&A, 77, 145

Monet D. G. et al., 2003, AJ, 125, 984

Olech A., Moskalik P., 2009, A&A, 494, L17

Paczyński B., 2000, PASP, 112, 1281

Paczyński B., Szczygieł D. M., Pilecki B., Pojmański G., 2006, MNRAS, 368, 1311

Pashchenko I. N., Sokolovsky K. V., Gavras P., 2018, MNRAS, 475, 2326

Pawlak M. et al., 2016, Acta Astron., 66, 421

Payne Gaposchkin C. H., Gaposchkin S., 1938, Ann. Astrophys., 1, 430

Payne-Gaposchkin C., 1978, ARA&A, 16, 1

Pedregosa F. et al., 2012, preprint (arXiv:1201.0490)

Percy J. R., Colivas T., 1999, PASP, 111, 94

Pietrzyński G. et al., 2013, Nature, 495, 76

Pojmanski G., 2002, Acta Astron., 52, 397

Pojmanski G., 2003, Acta Astron., 53, 341

Pojmanski G., Maciejewski G., 2004, Acta Astron., 54, 153

Pojmanski G., Maciejewski G., 2005, Acta Astron., 55, 97

Pojmanski G., Pilecki B., Szczygiel D., 2005, Acta Astron., 55, 275

Poleski R., 2014, PASP, 126, 509

Roeser S., Demleitner M., Schilbach E., 2010, AJ, 139, 2440

Rucinski S. M., 1992, AJ, 103, 960

Rucinski S. M., Pribulla T., van Kerkwijk M. H., 2007, AJ, 134, 2353

Samus' N. N., Kazarovets E. V., Durlevich O. V., Kireeva N. N., Pastukhova E. N., 2017, Astron. Rep., 61, 80

Sandage A., Tammann G. A., 2006, ARA&A, 44, 93

Scargle J. D., 1982, ApJ, 263, 835

Schwarzenberg-Czerny A., 1996, ApJ, 460, L107

Shappee B. J. et al., 2014, ApJ, 788, 48

Skrutskie M. F. et al., 2006, AJ, 131, 1163

Sobel D., 2017, The Glass Universe. Penguin Books, London

Soszynski I., Udalski A., Kubiak M., Szymanski M., Pietrzynski G., Zebrun K., Szewczyk O., Wyrzykowski L., 2004, Acta Astron., 54, 129

Soszynski I. et al., 2007, Acta Astron., 57, 201

Soszyński I. et al., 2015, Acta Astron., 65, 297

Soszyński I. et al., 2016, Acta Astron., 66, 405

Soszyński I., 2017, Acta Astron., 67, 103

Steele I. A., 2017, Astron. Telegram, 10713

Stellingwerf R. F., 1978, ApJ, 224, 953

Stetson P. B., 1996, PASP, 108, 851

Torres G., Andersen J., Giménez A., 2010, A&AR, 18, 67

Udalski A., 2003, Acta Astron., 53, 291

Vardya M. S., 1988, A&AS, 73, 181

Watson C. L., Henden A. A., Price A., 2006, in Lock B., ed., Society for Astronomical Sciences Annual Symposium, Vol. 25. Society for Astronomical Sciences, Rancho Cucamonga, CA, p. 47

Whitelock P. A., Feast M. W., Van Leeuwen F., 2008, MNRAS, 386, 313

Williams P. K. G., Clavel M., Newton E., Ryzhkov D., 2017, Astrophysics Source Code Library, ascl:1704.001

Windmark F., Lindegren L., Hobbs D., 2011, A&A, 530, A76

Woźniak P. R. et al., 2004, AJ, 127, 2436

Zacharias N., Monet D. G., Levine S. E. et al., 2004, BAAS, 36, 48.15

Zacharias N., Finch C. T., Girard T. M., Henden A., Bartlett J. L., Monet D. G., Zacharias M. I., 2013, AJ, 145, 44

Zechmeister M., Kürster M., 2009, A&A, 496, 577

Zhevakin S. A., 1963, ARA&A, 1, 367

This paper has been typeset from a TEX/LATEX file prepared by the author.